Author version: *Geochim. Cosmochim. Acta, vol.145; 2014; 139-158*

Chemistry and petrology of Fe–Ni beads from different types of cosmic spherules: Implication for precursors

N. G. Rudraswami[1*], M. Shyam Prasad[1], E. V. S. S. K. Babu[2], T. Vijaya Kumar[2]

[1]National Institute of Oceanography (Council of Scientific and Industrial Research), Dona Paula, Goa 403 004, India

[2]National Geophysical Research Institute, (Council of Scientific and Industrial Research), Hyderabad 500 007, India

*Corresponding Author: rudra@nio.org

Abstract

Fe–Ni beads are observed to occur in all three (Stony, Glass, Iron) types of cosmic spherules collected from deep sea sediments of the Indian Ocean. Fe–Ni beads in cosmic spherules can provide insights for understanding metal segregation mechanisms and their refractory metal element (RME: Re, Os, W, Ir, Ru, Mo, Pt, Rh including Pd) compositions can help ascertain their precursor meteorites. We measured RME compositions of 55 Fe–Ni beads using LA-ICP-MS in all three basic types of cosmic spherules selected after examining ~2000 cosmic spherules. The RMEs of Fe–Ni beads provide unique information on formation and differentiation during atmospheric entry. The variability in the concentration of the RMEs depends on the initial mass of the cosmic spherules, volatility, temperature attained and efficiency in metal segregation during entry. The CI chondrite and Os normalized RME compositions of the beads display a pattern that is close to CI chondritic composition. The presence of Pd, a non-refractory metal having condensation temperature similar to Fe, in Fe–Ni beads of all types of cosmic spherules indicates that the heating undergone was below its vaporization temperature. Not all parent bodies lead to the formation of beads, the precursor needs to exceed a certain minimum size and temperature to facilitate the metal to get segregated into beads. The minimum size of a parent particle that could enclose a Fe–Ni bead is estimated to have a size ~1 mm. This places constraints on the sizes of materials that are ablated during entry, and the accompanying mass loss during entry. Our study further points out that all the three basic types of cosmic spherules have a chondritic origin based on their RME distribution patterns. Only metal-rich carbonaceous chondrites contain the required quantities of metal for the formation of Fe-Ni beads during atmospheric entry and during this process the RMEs are also efficiently segregated into these beads.

1. INTRODUCTION

Micrometeorites are small dust particles with sizes ranging from tens of micrometers to ~2 mm, carry valuable information related to our understanding of the early solar system. Most of the dust is derived from the asteroid belt. An unknown fraction is of cometary origin. The total annual flux of micrometeorites is in the range of a ~few thousands to 40,000 tons, out of which >90% is evaporated before reaching the Earth's surface (Love and Brownlee, 1991, 1993; Taylor et al., 1998; Peucker-Ehrenbrink and Ravizza, 2000; Vondrak et al., 2008). Estimates of dust contribution from comets show large variation from ~25% (Kortenkamp and Dermott, 1998) up to ~85% of the total flux. Most of the cometary contribution may come from the Jupiter family comets (Nesvorný et al., 2010). Micrometeorites that impact the top of the atmosphere at an altitude of ~120 km undergo heating depending on the mass, zenith angle, entry velocity and the chemical composition (Love and Brownlee, 1991, 1993; Flynn, 1989). The micrometeorites are unmelted or partially melted if the mass and entry velocity are smaller, and the zenith angle is larger thereby, helping in preserving the original mineralogical composition (Kurat et al., 1994). Most of the micrometeorites are heated to such an extent that they lose some of their original chemical composition due to vaporization making it difficult to relate their chemistry to their precursors. The chemistry of ~500 S-type (stony) cosmic spherules collected from deep-sea, stratosphere and Antarctica studied for major and minor elements show loss of siderophile and volatile elements, such as Na and S during atmospheric entry. Non-volatile elements such as Mg, Al, Ca, Ti, Cr, and Mn were not lost. They have concentrations similar to those in CM chondrites (Brownlee et al., 1997). This is also supported by laboratory simulation experiments for mass loss (Hashimoto, 1983; Toppani et al., 2001).

Cosmic spherules are broadly classified into I (iron), G (glass) and S (Stony) types based on their chemical and textural characteristics (Blanchard et al., 1980; Brownlee et al., 1997; Genge et al., 2008). The I-type spherules are dominated by wustite (FeO) and magnetite (Fe_3O_4) phases and sometimes show the presence of Fe–Ni metal beads or refractory metal element (RME: Re, Os, W, Ir, Ru, Mo, Pt, Rh including Pd) nuggets (Brownlee et al., 1984; Rudraswami et al., 2011). The G-type spherules have textures characterized by dendritic magnetites in silicate rich glassy groundmass. Their chemical compositions show a large spread, between I-type and S-type spherules. Most G-type spherules contain Fe–Ni metal beads, rarely RME nuggets (Rudraswami et al., 2014). The S-type spherules are further sub-divided depending on the thermal reprocessing undergone during atmospheric entry (Genge et al., 2008). The I- and G-type spherules occur in low percentages in unbiased collections (~1–3%) whereas, the barred spherules among the S-type spherules are

dominant, close to 50% of the total number of micrometeorites (Taylor et al., 2000; Yada et al., 2004; Suavet et al., 2009; Prasad et al., 2013). While Fe–Ni beads are common among the I- and G-type spherules, they are found in only few S-type spherules (Brownlee 1985; Taylor et al. 2000).

Fe–Ni beads were observed, for the first time, in cosmic spherules over a century ago and were assigned a cosmic origin (Murray and Renard, 1891). Subsequently Fe–Ni bead bearing I-type spherules were identified as oxidized Fe–Ni alloy having a 'nucleus' where the Ni and Co contents were found to be meteoritic and the iron was suggested to be preferentially oxidized (Castaing and Fredriksson, 1958; Hunter and Parkin, 1960). Finkelman (1970) extracted I- and G-type spherules from manganese nodules both having beads, suggesting that the I-type spherules could have originated from iron meteorites whereas the G-type spheres were ablation products of stony meteorites. Fe–Ni beads generated during ablation experiments on iron meteorites (Blanchard and Davis, 1978) were found to have similar compositions as I-type spherules in possessing Fe–Ni bead along with magnetite and wustite, and hence they were assigned an origin of ablation from metal-rich meteoroids (Blanchard et al., 1980). The glass spherules were suggested to be the end products of intense vapour fractionation of silicate or metal-rich silicate meteoroids (Blanchard et al., 1980) where the Fe–Ni beads were subsequently separated from the parent meteoroids due to the density differences during atmospheric entry (Brownlee et al., 1983). Fe–Ni beads were also found in S-type spherules, Ni is quantitatively concentrated in the beads (Brownlee 1985; Taylor et al., 2000).

As most of the cosmic spherules have carbonaceous chondrites as precursors, the carbon during atmospheric entry burns giving rise to a reducing environment within the particle where the metal segregates into a Fe–Ni bead and often separates from the host (Brownlee et al., 1997). This bead is the precursor for the I-type spherules, which upon subsequent oxidation during the entry process, leads to the formation of wustite and magnetite in varying combinations (Brownlee et al., 1984). Heating of the spherules and successive formation of Fe–Ni beads combined with fast cooling, would lead to trapping of beads in the S-type cosmic spherules before it can become an independent identity. A metallic bead is observed in all three types of spherules due to incomplete oxidation, whereas complete oxidation and heating would further lead to the formation of RME nuggets which were earlier found in I-type spherules (Brownlee et al., 1984), but more recently have been reported from all the three types of spherules (Rudraswami et al., 2011, 2012, 2014).

The origin of I-type spherules still needs to be clarified. The I-type spherules have been understood to be the oxidized Fe–Ni beads released from ablating S-type spherules (Brownlee et al. 1984). Genge and Grady (1998) predicted that the larger sized spherules in sizes up to 400 μm have

the potential to produce beads in the sizes of ~30 μm which should be found in large numbers. The finding of cosmogenic radionuclides in I-type spherules further suggested that they are primary entities which are parts of metal-rich chondritic bodies (Herzog et al. 1999). Whereas, the G-type spherules have been enigmatic and their precursors are not clearly known, while several possibilities have been offered such as metal-rich silicate meteorites (Blanchard et al. 1980); stony-iron type parent body (Robin et al., 1988); enstatite chondrites (Bates, 1986) or enstatite-metal-rich asteroid or fine-grained C-type asteroids (Brownlee et al., 1997). Fe–Ni metal bead formation process appears to be common for all the three basic types of cosmic spherules. Further, RMEs are the most refractory of all metals and their precursor signatures are therefore expected to survive the rigors of atmospheric entry, therefore investigation of the RMEs in these beads could further our understanding on the origin and formation of the different types of spherules and the mechanism of metal segregation.

We investigated ~2000 cosmic spherules for Fe–Ni beads from the Indian Ocean collected by two different methods: by magnetically raking the seafloor (Parashar et al., 2010) and also magnetic separation from bulk sediments collected by seafloor grab samplers (Prasad et al., 2013). Out of ~2000 spherules investigated, we identified and analyzed 55 Fe–Ni bead containing spherules among all the three basic types of cosmic spherules to provide clarity on their origin, identify their precursors and understand their process of formation and metal segregation. Understanding the platinum group element (PGE) abundance and their inter-element ratios in the beads and in the remaining portions of spherules provides insights into heating during atmospheric entry, parent bodies that the spherules have evolved from, and an estimate of the initial size of the spherules before they impact the Earth's atmosphere. In addition, spherules without beads were also analyzed for PGE abundance and elemental distribution patterns for an effective comparison.

2. DEEP SEA SEDIMENT SAMPLES

Cosmic spherules in the present study were collected during five 35–day cruises in the Indian Ocean by two different methods: (1) Magnets fixed to a dredge which was dragged across the seafloor as detailed in Parashar et al. (2010). This is a magnetically biased collection and has shown a dominance of I- and G-type spherules. (2) One hundred close-spaced Okean Grab (Russian design of Van Veen grab) sampling operations were carried out during two cruises of 35 days each in the Indian Ocean. At each of these locations, ~30–45 kg of sediment was recovered and a total quantity of ~3000 kg of deep sea sediment was sieved in all the 100 locations using a 200 μm mesh size. The sieved and dried coarse fractions were magnetically separated and spherules were handpicked from

these magnetic fractions using the binocular microscope. This constitutes an unbiased collection (Prasad et al., 2013). The isolated spherules were cleaned with distilled water using ultrasonic bath. Later they were dried and handpicked by observing under the optical microscope and mounted on epoxy. Cosmic spherules were then identified after generating polished sections by observing under the scanning electron microscope (SEM) with an EDS (energy dispersive x-ray analysis system). For this investigation polished sections of >2000 spherules (~150–300 μm in size) mounted on nearly 15 epoxy mounts, picked from ~30 close-spaced locations in the Indian Ocean are examined for the presence of Fe–Ni beads. Three sediment cores were collected in the area to ascertain the terrestrial age of the spherules. By using the peak of abundance of Australasian microtektites in the cores as a chronostratigraphic unit of 0.77 Ma, the terrestrial age of the micrometeorites in the study have a timescale of ≤50,000 years (Prasad et al., 2013).

3. ANALYTICAL TECHNIQUES

Carbon coated polished sections were observed under scanning electron microscope (SEM) JEOL JSM 5800LV attached with OXFORD-INCA energy dispersive spectrometer detector (EDS, ISIS–300) system at National Institute of Oceanography, Goa. Electron beam energy of 20 keV was used for back-scattered electron (BSE) images. Suitable high resolution BSE images were inspected to identify the presence of Fe–Ni beads in the selected samples. Subsequently, the composition of the Fe–Ni beads and the bulk chemical compositions of the spherules were obtained using an electron probe micro-analyzer (EPMA, Cameca SX–5) having four spectrometers at the National Institute of Oceanography, Dona Paula, Goa. The parameters used for EPMA are: acceleration voltage of 15 kV, a beam current of 12 nA and beam diameters of ~2 and 5 μm for Fe–Ni bead and bulk chemical compositions, respectively. Concentrations of eleven elements (Na, Mg, Si, Al, P, K, Ca, Ti, Cr, Fe, Mn) were measured during the analysis. Multiple analyses were done depending on the size of the bead and the spherule. The data reduction and correction was done using PAP model (Pouchou and Pichoir, 1991).

Refractory metal elements were studied using a New Wave UP213 nm Laser Ablation system with a Thermo X SeriesII inductively coupled plasma mass spectrometer (LA-ICP-MS) at the National Geophysical Research Institute (NGRI), Hyderabad. Focused Nd:YAG laser beam on a continuous mode with an ablation time of ~150 s and a repetition rate of 10 Hz produces a pit of ~30–40 μm and an energy of ~2.5 mJ. The isotopes measured were as follows: ^{62}Ni, ^{95}Mo, ^{101}Ru, ^{103}Rh, ^{105}Pd, ^{182}W, ^{185}Re, ^{189}Os, ^{193}Ir, ^{195}Pt, ^{197}Au. SRM 610 (National Institute of Standards and Technology) and BCR-2G (US Geological Survey) were used for tuning and monitoring the

sensitivity of the instrument. Internal elemental standard used in the study was Ni. Three iron meteorites Filomena (IIA), Hoba (IVB) and Cape York (IIIAB) were used as running standards for the measurement of RMEs (PGEs, Re, Mo, W) in the Fe–Ni beads (Pataev and Jacobsen, 2004). 6–8 analyses on Fe–Ni beads or silicates of cosmic spherules are bracketed by ~6 standard analyses of Hoba. Filomena and Cape York were included as unknowns in each session to monitor reproducibility. The LA-ICP-MS measurements of PGEs, Re, Mo and W have an error < 8–10 % (1σ), based on repeated measurements of the Filomena and Hoba standards. After analyses, each spot was re-examined by SEM to identify the position of analyzed spot and pit size. This allowed us to do away with irregular pits of laser, and also to make sure that we have targeted the desired phases on the spherules accurately.

4. RESULTS

4. 1. Physical Properties

Fe–Ni beads in I-type spherules are observed to have the largest diameters among all the three types of spherules (Figs. 1–3). The beads are nearly spherical in shape and in a majority of the cases they are eccentric, located close to the edge of the spherule. This is different from the spherules having μm sized RME nuggets which were found scattered in all parts of the spherules (Rudraswami et al., 2014). Generally, the diameter of the Fe–Ni bead is found to increase with the increase in spherule diameter, this is found to be true for all the spherules (Fig. 4). However, the reverse is true many times in I-type spherules, where smaller sized spherules contained Fe–Ni beads which occupy more than half of the spherule diameter. The beads in S-type spheres have sizes in the range ~72–153 μm thereby contributing ~2–5 vol%. The G-type spherules have Fe–Ni beads in the size range of ~47–140 μm contributing ~1–30 vol%. However, beads in the I-type spherules have a size range of ~44–214 μm contributing ~1–52 % of the total volume of the spherules.

4. 2. Bulk chemistry

The bulk chemistry of the I-type spherules is dominated by magnetite and wustite phases. These phases are formed by high temperature interaction with oxygen in the atmosphere. The fractions of magnetite and wustite phases differ from spherule to spherule depending on the length of time it has experienced heating, temperature and oxygen fugacity. Bulk major element chemistry of the entire suite of I-type spherules having Fe–Ni beads show variations in abundances of FeO ~89–99 wt% and NiO ~0–9 wt% (Table 1). Co is also present in many I-type spherules up to a maximum of 0.5 wt% as an oxide. I-type spherules enclosing larger Fe–Ni beads have low concentration of the magnetite

phase. With the reduction in the Fe-Ni bead size a complimentary increase in the magnetite phase is seen suggesting most of the original metal has been oxidized. Bulk major element chemistry of G-type spherules that contain beads is as follows: FeO~55–98 wt%, NiO ~0.1–0.6 wt%, MgO ~0.3–25 wt%, SiO_2 ~1–27 wt%, Al_2O_3 ~0.1–1 wt% and CoO up to ~0.1 wt%. The S-type spherules with beads are barred and have silicate bulk chemistry enriched in FeO ~34–51 wt%, SiO_2 ~29–37 wt% and MgO ~15–26 wt%. A majority of the Co versus Ni data of the beads in S-, G-, I-type spherules are scattered close to chondritic line (Fig. 5). At lower Co and higher Ni values deviations from the chondritic ratio are significant. Nevertheless, a majority of Co and Ni concentrations of the Fe–Ni beads in all type of spherules overlap with each other.

4. 3. Chemistry of Fe–Ni beads

We identified 55 cosmic spherules with beads. Out of which, 5 are barred S-type, 23 are G-type, 27 are I-type spherules, respectively. The chances of finding Fe–Ni beads in each of the spherule types are very small. When we look at unbiased sampling carried out with the okean grab sampler where the total area and volume sampled are known, it is seen that the I-type spherules constitute ~5% of the total collection and beads are observed in <20% of the I-type spherules. This constitutes ~1% of the total collection. The statistics are similar for the G-type spherules which constitute ~3% of the total number of spherules. Among the S-type spherules, only barred spherules show beads in this collection. The percentage of spherules having beads among the barred spherules is extremely low, out of >500 barred spherules observed only 5 contain a metallic bead, which constitutes <1% of the total collection. All the above descriptions are valid for the unbiased collection observed by us (Prasad et al., 2013) and the extended investigations on our unbiased collection for the present study. These statistics assume importance when computing the entry conditions, pre-atmospheric entry sizes of meteoroids etc. as discussed in a further section of this manuscript. For the magnetically biased collection, similar to the one presented in Parashar et al. (2010), I-type spherules dominate with ~35% and the G-type spherules make up ~5% of all magnetic spherules. Here we could find many I-type spherules which contained a bead.

4.3.1 S-type spherules

Barred spherules with beads range in diameter from ~69 to 153 μm (Fig. 1). The chemical composition of the beads revealed a range in composition: Fe ~24–74 wt%, Ni ~26–76 wt% and Co up to 2 wt% (Table 1). Cobalt is observed in all the beads in S-type spherules, except for AAS-D4-#1L-P4. The RME analyses of Fe–Ni bead normalized to CI and Os values are nearly chondritic, except for depletions at W and Mo (Fig 6). Although W and Mo are refractory metals they can be

easily oxidized and transported into the silicate melt. The extent of depletion will depend on the amount of oxygen available (Palme et al., 1994). Different elemental ratios (Os/Ir, Ru/Ir, Rh/Ir, Pd/Ir, Pt/Ir, Pt/Os, Pt/Rh, Pt/Ru and Pt/Pd) normalized to CI values do not deviate strongly from chondritic ratios (Fig. 6). The absolute concentration of the RME in the beads is much higher than in chondrites. The enrichment of PGEs is more than hundred times that of CI chondrites (Table 2).

4.3.2 G-type spherules

Beads in G-type spherules have a size range ~46–140 μm which is similar to those in S-type spheres (Fig. 2). The chemistry of Fe–Ni beads in G-type is no different from that of the beads in the S-type spherules. The beads have a wide range in chemical composition: Fe ~8–79 wt%, Ni ~19–93 wt% and Co ~1–3 wt% (Table 1). The concentration of Co is higher than that of the beads found in S-type spherules. The plot of Ni versus Co of the beads in many G-type spherules falls within the chondritic range (Fig. 5). Ni also dominates in a majority of the beads. LA-ICP-MS studies on Fe–Ni beads of the G-type spherules were done to know the RME concentration. The RME concentration of the beads normalized to CI and Os values in the G-type spherules are clustered near CI chondritic values except for W and Mo as can be seen in Fig. 7. Some of the analyses on the remaining portions of the spherules show depletion in PGEs below the detection limit of the instrument. The details of the PGE concentration in the beads and in the remaining portions of the spherules are given in Table 2 and 3, respectively.

G-type spherules without beads were also analyzed to compare with those having a bead (Table 4). The concentration of the RME in G-type spherules without a bead was much lower than compared to that with beads (Table 2 and 4). The most refractory elements Os and Ir are depleted ~100 times relative to CI values in these spherules. The CI and Os normalized values of the RMEs in the G-type spherules without beads are close to CI values, except for elements like W and Mo (Fig. 8a). The elemental ratios are close to chondritic compositions (Fig.8b).

4.3.3 I-type spherules

Beads in I-type spherules are considerably larger with a diameter range of ~44–214 μm (Table 1). Some of the beads constitute as high as ~52 % of the spherule by volume, and this is much higher compared to beads in S- and G-type spherules. Often beads in I-type spherules are located closer to the edge of the spherules. Usually single Fe–Ni beads are found, however, there are few spherules with multiple Fe–Ni beads. In such cases, the size of the bead is too small for laser beam analyses. The chemical composition of the beads shows an Fe range ~6 to 88 wt%, Ni ~10 to 93 wt%, and Co

~0.2 to 4.4 wt%. The Ni versus Co of Fe–Ni beads in I-type spherules is widespread as shown in Fig. 5. The LA-ICP-MS studies on Fe–Ni beads of the I-type spherules (RME composition normalized to CI chondrite and Os values) show elemental ratios close to chondritic values, this is also true for elemental ratios normalized to CI chondritic values (Fig. 9). The analyses on the beads show enrichment and whereas the rest of the spherules are depleted in PGE similar to those seen in G-type spherules (Table 2 and 3).

PGE analyses of I-type spherules without beads show depletion similar to G-type spherules which do not have beads (Table 4). The PGE distribution patterns in the general area of the spherules are scattered and not smooth, unlike as observed in the Fe–Ni beads of I-type spherules (Fig. 10). This indicates that the I-type spherules which have released the Fe–Ni beads have undergone complete oxidation forming wustite and magnetite, and probably also crossed the stage of nugget formation where the entire PGE of the spherules will be segregated and concentrated in small nuggets. Those PGE in the beads deviating from the chondritic pattern may be due to inefficient segregation of PGEs, or loss of PGEs during atmospheric heating and sometimes also due to the presence of nuggets rich in PGEs hidden below the region of analyses.

5. DISCUSSION

If each or group of cosmic spherules represents an individual or different groups of asteroids, the chemical differences between dissimilar spherules are obliterated due to frictional heating during the atmospheric entry and so also the uniqueness of the asteroid they belong to. Achondrites have very low Co and Ni contents (Lodders and Fegley, 1998) suggesting that the S-, G- and I-type spherules analyzed in the present study are mostly chondritic. Similarly, non-chondritic Ni/Co ratios in most iron meteorites (Kelly and Larimer, 1977) makes them an unlikely source. Iron meteorites as precursors can also be excluded on the simple premise that in view of the tensile strength of the Fe–Ni metal they do not seem to fragment so easily to form dust. The important attributes of the PGE data from Fe–Ni beads and spherules of S-, G- and I-type is to unravel the processes that have taken place during atmospheric entry. The PGE concentration in beads helps in understanding the mass loss, formation process of bead and finally, if possible, relation to known chondritic parent bodies. Not all parent bodies lead to the formation of beads as temperature and initial size play a prominent role in its formation.

5.1. Precursor dimension, mass loss and Fe–Ni bead formation

The dust particle that enters the Earth's atmosphere undergoes heating and attains peak temperatures depending on various parameters like mass, zenith angle, entry velocity and chemical composition (Love and Brownlee, 1991; Vondrak et al., 2008). The micrometeorite entering at velocity >11 km/s and low zenith angle impacts the atmosphere at ~120–140 km above the earth's surface. This generates sufficient heat due to friction with air molecules producing the required temperature to change its mineralogical composition (Love and Brownlee, 1991; Vondrak et al., 2008). As a consequence, coalescing of metals and silicate takes place separately due to immiscibility and large differences in their densities. ~~The~~ Micrometeorites heated to >1500 ^{o}C undergo textural and chemical changes including mass loss making it difficult to relate them to specific meteorite parent bodies. Brownlee et al. (1984) predicted a sequence of events where the dust particles due to frictional heating above the silicate solidus, facilitate molten metal to segregate and differentiate from the silicate components due to large density differences, similar to differentiation events in planetesimals. Chemical affinity of the PGEs towards metal and high metal silicate partition coefficient ($D>10^4$) during the molten stage move all metal into Fe–Ni metal phases. Continuation of the process of heating and oxidation during entry leads to nugget formation leaving the silicate portion completely depleted of PGEs (Brownlee et al., 1984). Extended heating in air will lead to increased evaporation and oxidation, both of which cause the core to shrink. Ni correlates positively with the PGE in the beads, and the high concentration of PGE in beads, suggest Fe evaporation during the process (Fig. 11). I-type spherule formation was argued to have formed by ejection of Fe–Ni beads from the molten silicate spherules originating from chondritic parent bodies, alternatively as metal from carbonaceous chondrites (Brownlee et al., 1984; Herzog et al., 1999). Iron meteorites were also related to I-type spherules based on concentration of ^{10}Be (Yiou et al., 1985). The concentration of the volatile PGE like Pd in the iron meteorites is low (Petaev and Jacobsen, 2004) compared to what we found in Fe–Ni beads of S-, G- and I-type cosmic spherules. The high abundances of volatile and refractory PGEs in beads can be considered as an important criterium that rules out iron meteorites as their precursors. However, refractory metal abundance/Pd ratios are also chondritic in some iron meteorites. The type IAB iron meteorites have in general chondritic pattern siderophile elements and would be certainly candidates for metal beads (Kelly and Larimer, 1977). The Cr/Fe ratios of I-type spherules are comparable with those of metal from CM, CO, CV, CR carbonaceous chondrites, unlike the iron meteorites which have very low Cr/Fe ratio (Yiou et al., 1985; Herzog et al., 1999). In addition, the Fe/Ni ratios of I-type spherules and carbonaceous chondrites are comparable (Herzog et al., 1999). The PGE in Fe–Ni beads of cosmic

spherules are enriched several orders of magnitude when normalized to CI chondrites. For e.g. the enrichment of Os in the beads of S-type spherules varies from ~4–140 × CI, in G-type varies from ~5–1080 × CI, while those in I-type vary from ~4–1500 × CI chondrites (Table 2). The high PGE enrichment in I-type spherules as compared to G- and S-type spherules is probably due to higher PGE contents in the original beads and the greater efficiency of removal of PGE from a metal source due to differences in oxidation potential between the Fe–Ni and the PGE. Some of the analyses done on the silicate or remaining portions of cosmic spherules (apart from Fe–Ni bead) shows total PGE depletion, thereby demonstrating an efficient segregation mechanism of PGEs in beads within a short span of time during atmospheric entry (Table 3).

The enrichment of PGE in the metal beads of cosmic spherules is very high (Table 2). If the PGE come from a chondritic parent body, oxidation or evaporation of Fe must have produced the enrichment of PGE in the metal beads. The PGE concentration in CI is known (Tagle and Berlin, 2008), and the micrometeorite spherule is assumed to have homogeneous PGE concentration with known CI composition. Also most of the bulk PGE in chondrites is in similar proportions except for a few chondrites like CH and CB that have higher PGE contents (Tagle and Berlin, 2008). The total PGE contained in a bead is X amount. Assuming that the parent body were a carbonaceous chondrite, calculations were made to understand what would be the total size of a meteoroid that was ablated in order for X amounts of PGE to be efficiently concentrated in the bead. Therefore, the total mass of PGE contained in the bead is extrapolated to arrive at the mass of a precursor carbonaceous chondrite. The estimates are carried out on the CI composition precursor. It can be seen that Fe–Ni beads with smaller sizes tend to have increased PGE concentration compared to those with larger diameters for the same initial size of host spherule (Fig. 12). Continued heating of the Fe–Ni beads would have developed into nuggets as Fe would have been further vaporized facilitating the high siderophile RME to form into nuggets. The vaporization of Fe will also result in vaporization of Pd which has a similar condensation temperature (Campbell et al., 2001). Ni and Co are more refractory compared to Fe, the increase in concentration of Ni should also reduce the concentration of Pd. Fig. 12 provides an estimate of the initial size of the micrometeorite body before it impacts the top of the atmosphere. These extrapolations suggest that the radius of the cosmic spherules before entry needs to be ~3–5 times the recovered spherule size to account for the amount of PGEs found in the Fe–Ni beads. This also indicates that >80% of the initial mass is lost as it enters the Earth's atmosphere. The larger the size of the particle during the entry, more PGE gets accumulated into the bead if the particle receives the right temperature. Also it is equally true that smaller beads with large entry size spherules also can accumulate larger concentration of PGEs due to evaporation of Fe and Ni. We

suggest that most of the cosmic spherules with Fe–Ni beads have sizes close to ~1 mm before entering the Earth's atmosphere.

The average size of micrometeorites entering the earth that survive atmospheric entry as per most estimates is ~200 μm (Love and Brownlee, 1993; Taylor et al., 2000; Yada et al., 2005). Larger sizes of micrometeorites are rare because they need to enter at very high zenith angles, and should have the appropriate chemical compositions that do not vaporize easily, such larger particles constitute the extreme large diameter end of the spectrum of micrometeorite dimensions and are close to or less than 1% of all particles entering the atmosphere (Love and Brownlee 1993; Greshake et al., 1998). Van Ginneken et al. (2012) provided detailed mineralogical studies on eight large micrometeorites from Antarctica in the sizes >300 μm to ~1mm, out of which particles were observed to have an ordinary chondrite and the others a carbonaceous chondrite precursor. Further, oxygen isotope analyses done on large micrometeorites also suggest ~30 % of these particles are related to ordinary chondrites (Suavet et al., 2010). This is not true for the oxygen isotope analysis done on smaller sized (~200 μm) micrometeorites using an ion microprobe (e.g. Engrand et al., 1999; Yada et al., 2005; Matrajt et al., 2006). Disruptive collisional forces in the asteroid belt produce more dust in the size range of tens of micrometers to 200 μm in hydrous bodies when compared with anhydrous asteroids suggesting large sized micrometeorites can be contributions from ordinary chondrites, while those in smaller sizes are largely dominated by comminution products of carbonaceous chondrites (Van Ginneken et al., 2012).

5.2 Parent bodies of Fe–Ni bead bearing cosmic spherules

Fe–Ni metal is commonly present within the chondrules and matrices of many carbonaceous chondrites. Most of the chondrules in CR chondrites show large amounts of metals which occupy ~5–8 vol%, these metals show positive Ni versus Co correlation (Grossman et al., 1988; Weisberg et al., 1995; Choe et al., 2010; Wasson and Rubin, 2010). The concentration of Ni in metals of CR chondrites is in the range ~5–22 wt%, however during atmospheric heating Fe which is more volatile would have evaporated resulting in Ni enrichment (Weisberg et al., 1995). These metals in chondrites may have contributed to the formation of I-type spherules. The chondrules in CR chondrites constitute up to ~55 vol% with an average size of ~700 μm, unlike those of CM chondrites which have an average diameter of ~270 μm (Choe et al., 2010). The chondrules in CV and CK chondrites are in the size range of ~800–1000 μm, however, the reduced CV chondrites contain metal up to ~5 vol%. Oxygen isotope data on many relict-grain bearing micrometeorites have shown a carbonaceous chondrite provenance (Yada et al. 2005; Taylor et al. 2005; Engrand et

al. 2005). Bulk oxygen isotopes on some of the large micrometeorites have shown ~30% of them relating to ordinary chondrites, and ~20–50% to CO/CV chondrites (Suavet et al., 2010). Major element chemistry of thousands of cosmic spherules analyzed provides a link to CM type carbonaceous chondrites, nevertheless, metal rich CR or reduced CV chondrites could also be related to Fe–Ni bead bearing cosmic spherules (Brownlee et al., 1997).

The Fe–Ni beads in cosmic spherules in spite of undergoing heating during atmospheric entry, the relative abundances of Ni and Co are well preserved with the result they plot close to the chondritic line (Fig. 5). The correlation between Ni and Co in the metal of carbonaceous chondrites (Weisberg et al., 1988, 1995) resembles to some extent that of Fe–Ni beads of all types of cosmic spherules, although there is scatter. Nevertheless a trend in favour of carbonaceous chondrites as a source for all bead forming spherules cannot be ruled out. The disintegration of carbonaceous chondrites into smaller particles similar in sizes to those of micrometeorites is feasible as they are hydrated and are lacking in mechanical strength (Tomeoka et al., 2003). Hypervelocity impact disruption experiments using a hydrated carbonaceous CM2 Murchison compared with anhydrous carbonaceous CV3 Allende and many ordinary chondrites suggest Murchison has an order of magnitude greater ability to produce dust in sizes <300 when compared with anhydrous meteorites (Flynn et al., 2009). The metal in carbonaceous chondrites such as CM, CO, CR, CH, CV_{red} can be viewed as plausible precursors for I-type spherules or even the G-type spherules. The Fe–Ni beads in S-type cosmic spherules may have originated from metal rich components already present in the dust particles of carbonaceous chondrites, where significant heating during atmospheric entry (≥1500 ^{o}C) has resulted in physical and chemical processing leading to spherical shapes, Fe vaporization and enrichment of Ni and PGE segregation from the silicate body into an Fe–Ni bead. The particle could have lost the silicates most likely after the PGE has segregated into the metal (Herzog et al., 1999). If already the metal is a part of the precursor then its initial size before atmospheric entry could be much smaller. The PGE data of Fe–Ni beads in spherules which are close to CI values along with a significant presence of the volatile element Pd supports the above mechanism. It is further possible that the bead formation within spherules could have originated from the metal existing in the carbonaceous chondrites based on Cr/Fe ratios which are comparable with metal in carbonaceous chondrites, rather than the bulk Cr/Fe ratios from meteorites (Herzog et al., 1999). The role of achondrites or iron meteorites in bead formation is unlikely as the present PGE data does not provide any supportive evidence. The volatile PGE contents of iron meteorites are very different from chondritic compositions, and their Cr/Fe does not fall in the range of micrometeorites, whereas the ratios for carbonaceous chondrites are quite close to those of micrometeorites (Herzog et al., 1999). Therefore,

it appears that bead formation is possible from specific carbonaceous chondritic precursors which are metal-rich such as the CM, CO, CV, CR, CH chondrites.

The PGE is abundant in S-, G- and I-type of cosmic spherules, but its concentration is more in I- and G-types when compared with the beads in S-type spherules. The precursors of S-type spherules have high ablation coefficients and do not travel deep into the atmosphere when compared with the I-type, and hence do not get heated for long durations (Janches and ReVelle, 2005). This may lead to incomplete segregation of PGE from the silicate body into the beads, in addition, faster cooling preserves some of the siderophile elements trapped in the silicate regions of the spherules. The PGE concentration in the beads far exceeds chondrite values although they have similar elemental ratios. The beads that are PGE-enriched have derived their PGE from the silicate regions into the bead as discussed above. The RME data on beads normalized to CI and Os from S-, G- and I-type spherules are close to chondritic, except in the case of elements like W and Mo. W and Mo can be more easily oxidized and tend to migrate into the adjoining silicate regions as oxides, this could be responsible for their depletion (Bischoff and Palme, 1987; Palme et al., 1994; Campbell et al., 2002). Less refractory elements like Pd are also not fractionated when compared to other PGEs, Re, Mo, W suggesting that the bead formation temperature has not crossed the Pd evaporation stage. In addition, normalization of elemental ratios (Os/Ir, Ru/Ir, Rh/Ir, Pd/Ir, Pt/Ir, Pt/Os, Pt/Rh, Pt/Ru, Pt/Pd) with CI values shows the ratios are close to chondritic compositions for all the three types of spherules (Fig. 6–7, 9). Therefore, it appears that a majority of the spherules with beads have a chondritic parent body. It may not be possible to pin point a particular type of chondrite, as a majority of the chondrites have PGE abundances similar to CI chondrite values (Tagle and Berlin, 2008). The G-type spherules were considered as intermediate between S- and I-type spherules (Blanchard et al., 1980). With slightly more heating and faster quenching S-type spherules will lose silicate and form magnetite dendrites thereby leading to the formation of G-type spherules with Fe–Ni beads. The chemical compositions of the G-type spherules show large variations and do not fall in the range of well-known meteorite groups (Brownlee et al., 1997). However, the Fe–Ni beads of G-type spherules have PGE compositions which are no different from those of the S-type or I-type spherules. This suggests that the G-type spherules have similar parent bodies as those of S- and I-type spherules. Apparently, the S-type spherules after entering the Earth's atmosphere experience heating and oxidation resulting in fractionation leading to the formation of the G-type spherules which upon further heating can form the I-type spherules. We found a spherule AAS-26-D32-M-P1 which has all the three possible phases (silicate, Fe-rich and Fe-Ni) which provides evidence for such a possibility (Fig. 13). Barred portion of this particle has FeO ~16 wt%, while the FeO of the

silicate area close to the bead has ~25 wt% suggesting an increasing trend of siderophile enrichment towards the bead and supporting the segregation mechanism. The silicate region close to the bead has textural features similar to those of G-type spherules, while the part of the spherule which is far from the bead resembles a barred spherule texture.

The plots of Fe–Ni beads from different types of cosmic spherules with different PGEs such as Os versus Ir, Ru, Rh and Pd show positive correlations similar to those seen in chondrites (Fig. 14). The plots are positively correlated for elements having similar condensation temperatures such as Os, Ir, and Ru, which is also true for refractory metal nuggets (Rudraswami et al., 2014). However, the refractory metal nuggets have negative correlation between volatile versus refractory PGEs which is not true in the case of Fe–Ni beads. This may be due evaporative loss of the elements in the nuggets. As the nugget formation enters the phase of extreme heating it may not be possible to retain all the volatile PGE which have condensation temperatures equivalent to those of Fe and Ni. Similarly, the plots of Rh versus Pd, Pt versus Pd, Ru versus Pt, and Os versus Pt are all positively correlated (Fig. 15). The plots of Re versus Os, Ir, Ru and Pt are also positively correlated (Fig. 16). This type of positive correlation is seen in chondrites. Slight spread from the trend in some of the elements may be due to differences in the diffusion levels of the PGEs, where all the PGE present in the spherules may not have been efficiently incorporated in to the beads. For example a deviation in the trend can be seen in some of the beads for Os versus Rh and Pd, Pt versus Pd, Re versus Pt (Figs. 14–16). However, increased heating leads to equilibration of refractory PGE and facilitates their partitioning into the beads, on other hand it also allows vaporization of volatile PGEs such as Rh, Pd and Pt resulting in deviation from expected chondritic values. This may not be true in RME nuggets which are not always positively correlated (Rudraswami et al., 2014). For example in RME nuggets Os versus Ru are negatively correlated. Nuggets are formed after exposing the particles to greater heating and for a longer duration than required for Fe–Ni bead formation, this would also result in significant vaporization of the volatile PGE elements like Pd, Rh and probably Pt. The negative correlation among the elements in RME nuggets is quite apparent (Rudraswami et al., 2014). The Fe–Ni beads have not undergone heating much beyond 1500 ^{o}C as they maintain the positive correlations between different elements of PGEs and Re (Fig. 14–16), unlike the nuggets that are exposed to temperatures >1700 ^{o}C to ~2500 ^{o}C which result in vaporization from Pd right up to Ru (Brownlee et al., 1984; Bonte et al., 1987; Rudraswami et al., 2014). The presence of beads suggests that oxidation in these bodies was not equivalent to that required for the formation of nuggets (Brownlee et al., 1984). The next stage of heating of the Fe–Ni beads results in loss of Fe and volatile PGEs leading to the formation of nuggets, nevertheless the elemental composition of

refractory PGEs are maintained close to chondritic values. The histograms of Fe–Ni beads for elemental ratios such as Os/Ir, Ru/Ir, Pt/Ir normalized to CI values are closer to ~1, but the ratios such as Pd/Ir and Pt/Ru are more scattered (Fig. 17). The ratio of Rh/Ir normalized to CI values is >1, indicating curtailed segregation of Ir.

6. CONCLUSIONS

We analyzed RMEs using LA-ICP-MS in 55 Fe–Ni bead bearing cosmic spherules encompassing all three basic spherule types. The Fe–Ni beads are enriched in PGE and the remaining portions of the cosmic spherules are depleted indicating that the siderophile elements have moved into the Fe–Ni bead – a process that has apparently taken place during their atmospheric entry. The present study supports atmospheric entry heating resulting in density separation between the metal and silicate fractions as suggested by Brownlee et al. (1984). Metal rich carbonaceous chondrites as precursors for bead formation in cosmic spherules appear to be a strong possibility. Normalized PGE data and the elemental ratios for Fe–Ni beads from all the three types of cosmic spherules (S-, G- and the I-type) have ~~a~~ patterns close to ~1 suggesting a chondritic origin. The calculations presented in this study suggest that in order to segregate the amount of PGEs observed in Fe–Ni beads, the size of the dust particle before it impacts the earth's atmosphere could be much larger than the average cosmic spherule size. Conversely, it may also be possible that if the precursors are enriched in metal, even smaller primary particles can lead to bead formation in spherules during entry. There are only few metal-rich carbonaceous chondrites that contain silicate and Fe–Ni contents that would qualify for appropriate parent bodies. The other meteorites do not have appreciable metal contents, or the elemental ratios rule out the rest such as the iron meteorites, achondrites, or mesosiderites.

ACKNOWLEDGEMENTS

The authors (NGR and MSP) are grateful to CSIR XII Plan funded Project GEOSINKS and Physical Research Laboratory, Ahmedabad, for the sanction of the PLANEX project on micrometeorites. We are indebted to Vijay Khedekar for his help in EPMA analyses and to Samena Balgar for the help in sample preparation. EVSSKB and TVK acknowledge the financial support from the CSIR 12th FYP Project INDEX WP-2.1 and MLP-6513-28-EVB. This is NIO's contribution No. xxxx.

REFERENCES

Bates B. A. (1986) The elemental composition of stony extraterrestrial particles from the ocean floor. Ph.D. thesis. University of Washington. 199 pp.

Bischoff A. and Palme H. (1987) Composition and mineralogy of refractory-metal-rich assemblages from a Ca, Al-rich inclusion in the Allende meteorite. *Geochim. Cosmochim. Acta* **51**, 2733–2748.

Blanchard M. B. and Davis A. S. (1978) Analysis of ablation debris from natural and artificial iron meteorites. J. *Geophys.Res*. **83,** 1793–1808.

Blanchard M. B., Brownlee D. E., Bunch T. E, Hodge P. W. and Kyte F. T. (1980) Meteoroid ablation spheres from deep-sea sediments. *Earth Planet. Sci. Lett.* **46**, 178–190.

Bonte Ph., Jehanno C., Maurette M. and Brownlee D. E. (1987) Platinum metals and microstructure in magnetic deep sea cosmic spherules. *J. Geophy. Res.* **92**, 641–648.

Brownlee D. E., Bates B.A. and Beauchamp R. H. (1983) Meteor ablation spheres as chondrule analogs. In *Chondrules and Their Origins*, ed. E.A. King, pp. 10–25, Houston: Lunar Planet. Inst.

Brownlee D. E., Bates B. A. and Wheelock M. M. (1984) Extraterrestrial platinum group nuggets in deep-sea sediments. *Nature* **309**, 693–695.

Brownlee D. E. (1985) Cosmic dust: Collection and research. *Annu. Rev. Earth Planet. Sci.*, **13**, 147–173.

Brownlee D. E., Bates B. and Schramm L. (1997) The elemental composition of stony cosmic spherules. *Meteorit. Planet. Sci.* **32**, 157–175.

Campbell A. J., Humayun M., Meibom A., Krot A. N. and Keil K. (2001) Origin of zoned metal grains in the QUE94411 chondrite. *Geochim. Cosmochim. Acta* **65**, 163–180.

Campbell A. J., Humayun M. and Weisberg M. K. (2002) Siderophile element constraints on the formation of metal in the metal-rich chondrites Bencubbin, Weatherford, and Gujba. *Geochim. Cosmochim. Acta* **66**, 647–660.

Castaing R. and Fredrickson K. (1958) Analyses of cosmic spherules with an X-ray microanalyzer. *Geochim. Cosmochim. Acta* **14**, 114–117.

Choe W. H., Huber H., Rubin A. E., Kallemeyn G. W. and Wasson J. T. (2010) Compositions and taxonomy of 15 unusual carbonaceous chondrites. *Meteorit. Planet. Sci*. **45**, 531–554.

Engrand C., McKeegan K. D. and Leshin L. A. (1999) Oxygen isotopic compositions of individual minerals in Antarctic micrometeorites: Further links to carbonaceous chondrites. *Geochimica et Cosmochimica Acta* **63**, 2623–2636.

Engrand C., McKeegan K.D., Leshin L.A., Herzog G.F., Schnabel C., Nyquist L.E. and Brownlee D.E. (2005) Isotopic compositions of oxygen, iron, chromium, and nickel in cosmic spherules: Toward a better comprehension of atmospheric entry heating effects. *Geochim. Cosmochim. Acta* **69**, 5365–5385.

Finkelman R. B. (1970) Magnetic particles extracted from manganese nodules. *Science* **167**, 982–984.

Flynn, G. J. (1989) Atmospheric entry heating: a criterion to distinguish between asteroidal and cometary sources of interplanetary dust. *Icarus* 77, 287–310.

Flynn J., Durda D.D., Minnick M.A. and Strait M. (2009) Production of cosmic dust by hydrous and anhydrous asteroids: implications for the production of interplanetary dust particles and micrometeorites. *Lunar Planet. Sci. LX*, #1164.

Genge M. J. and Grady M. M. (1998) Melted micrometeorites from Antarctic ice with evidence for the separation of immiscible Fe-Ni-S liquids during entry heating. *Meteorit. Planet. Sci.* **33**, 425–434.

Genge M.J., Engrand C., Gounelle M. and Taylor S. (2008) The classification of micrometeorites. *Meteorit. Planet. Sci.* **43**, 497–515.

Greshake A., Kloeck W., Arndt P., Maetz M., Flynn G. J., Bajt S. and Bischoff A. (1998) Heating experiments simulating atmospheric entry heating of micrometeorites: Clues to their parent body sources. *Meteorit. Planet. Sci*. **33,** 267–290.

Grossman J. N., Rubin A. E., Nagahara H. and King E. A. (1988). Properties of chondrules. *In Meteorites and the early solar system*, edited by Kerridge J. F. and Matthews M. S. Tucson, Arizona: The University of Arizona Press. pp. 619–659.

Hashimoto A. (1983) Evaporation metamorphism in the early solar nebula-evaporation experiments on the melt FeO-MgO–SiO_2-CaO-Al_2O_3. *Geochem. J.* **17**, 111–145.

Herzog G. F., Xue S., Hall G. S., Nyquist L. E., Shih C. Y., Wiesmann H. and Brownlee D. E. (1999) Isotopic and elemental composition of iron, nickel, and chromium in type I deep-sea spherules: implications for origin and composition of the parent micrometeoroids. *Geochim. Cosmochim. Acta* **63**, 1443–1457.

Hunter W. and Parkin D.W. (1960) Cosmic dust in recent deepsea sediments, *Proc. R. Soc. London* **255,** 382-397

Janches D. and ReVelle D. O. (2005) Initial altitude of the micrometeor phenomenon: Comparison between Arecibo radar observations and theory, *J. Geophys. Res.* **110**, A08307, doi:10.1029/2005JA011022.

Kelly W. R. and Larimer J. W. (1977) Chemical fractionations in meteorites—VIII. Iron meteorites and the cosmochemical history of the metal phase. *Geochim. Cosmochim. Acta* **41**, 93–111.

Kortenkamp S. J. and Dermott S.F.(1998) Accretion of interplanetary dust particles by the Earth. Icarus **135**, 469-495.

Kurat G., Koeberl C., Presper T., Brandstätter F. and Maurette M. (1994) Petrology and geochemistry of Antarctic micrometeorites. *Geochim. Cosmochim. Acta* **58**, 3879–3904.

Lodders K. and Fegley B (1998) The planetary scientist's companion, New York: Oxford University Press. 400 p.

Love S. G. and Brownlee D. E. (1991) Heating and thermal transformation of micrometeoroids entering the Earth's atmosphere, *Icarus* **89**, 26–43.

Love S. G. and Brownlee D. E. (1993) A Direct Measurement of the Terrestrial Mass Accretion Rate of Cosmic Dust. *Science* **262**, 550–553.

Matrajt G., Guan Y., Leshin L., Taylor S., Genge M., Joswiak D. and Brownlee D. (2006) Oxygen isotope measurements of bulk unmelted Antarctic micrometeorites. *Geochim. Cosmochim. Acta* **70**, 4007–4018.

Murray J. and Renard A.F. (1891) *Rep. Sci. Results Voyage H.M.S. Challenger 3*. Edinburgh : Neill and Co. 525pp

Nesvorný D., Jenniskens P., Levison H F., Bottke W. F., Vokrouhlický D,, and Gounelle M. (2010) Cometary Origin of the Zodiacal Cloud and Carbonaceous Micrometeorites. Implications for Hot Debris Disks. Astrophys. J. **713**, 816–836.

Parashar K., Shyam Prasad M. and Chauhan S. S. S. (2010) Investigations on a large collection of cosmic dust from the Central Indian Ocean. *Earth Moon Planet.* **107**, 197–217.

Palme H., Hutcheon I. D. and Spettel B. (1994) Composition and origin of refractory-metal-rich assemblates in a CaAl-rich Allende inclusion. *Geochim. Cosmochim. Acta* **58**, 495–513.

Petaev M. I . and Jacobsen S. B. (2004) Differentiation of metal-rich meteoritic parent bodies: I. Measurements of PGEs, Re, Mo, W, and Au in meteoritic Fe–Ni metal. *Meteorit. Planet. Sci*. **39**, 1685–1697.

Peucker-Ehrenbrink B. and Ravizza G. (2000). The effects of sampling artifacts on cosmic dust flux estimates: a reevaluation of nonvolatile tracers (Os, Ir). *Geochim. Cosmochim. Acta* **64**, 1965–1970.

Pouchou J. L. and Pichoir F. (1991) Quantitative analysis of homogeneous or stratified microvolumes applying the model "PAP". *In Electron Probe Quantification* (eds. K. F. J. Heinrich and D. E. Newbury). Plenum Press, New York, pp. 31–75.

Prasad M. S., Rudraswami N. G. and Panda D. K. (2013) Micrometeorite flux on earth during the last ~50,000 years. *J. Geophy. Res.***118**, 2381–2399.

Robin E., Jehanno C. and Maurette M. (1988) Characteristics and origin of Greenland FeMi cosmic grains. Proc. *Lunar Planet. Sci. Conf.* 18, 593–598.

Rudraswami N. G., Parashar K. and Shyam Prasad M. (2011) Micrometer and nanometer size platinum group nuggets in micrometeorites from the deep sea sediments of Indian Ocean. *Meteorit. Planet. Sci*. **46**, 470–491.

Rudraswami N. G., Shyam Prasad M., Babu E. V. S. S. K., Vijaya Kumar T., Feng W. and Plane J.M.C. (2012) Fractionation and fragmentation of glass cosmic spherules during atmospheric entry. *Geochim. Cosmochim. Acta* **99**, 110–127.

Rudraswami N. G., Prasad S. M., Plane J. M. C., Berg T., Feng W. and Balgar S. (2014) Refractory metal nuggets in different types of cosmic spherules. *Geochim. Cosmochim. Acta* **131**, 247–266.

Suavet C., Rochette P., Kars M., Gattacceca J., Folco L. and Harvey R. P. (2009) Statistical properties of the Transantarctic Mountains (TAM) micrometeorite collection. *Polar Science* **3**,100–109.

Suavet C., Alexandre A., Franchi I. A., Gattacceca J., Sonzogni C., Greenwood R. C., Folco L. and Rochette P. (2010). Identification of the parent bodies of micrometeorites with high-precision oxygen isotope ratios. *Earth Planet. Sci. Lett.* **293**, 313–320.

Tagle R. and Berlin J. (2008) A database of chondrite analyses including platinum group elements, Ni, Co, Au, and Cr: Implications for the identification of chondritic projectiles. *Meteorit. Planet. Sci*. **43**, *541-559.*

Taylor S., Lever J. H. and Harvey R. P. (1998) Accretion rate of cosmic spherules measured at the South Pole. *Nature* **392**, 899–903.

Taylor S., Lever J., and Harvey R. (2000). Numbers, types and compositional distribution of an unbiased collection of cosmic spherules. *Meteorit. Planet. Sci*. **35**, 651–666.

Taylor S., Alexander C. M. O'D., Delaney J., Ma P., Herzog G. F. and Engrand C. (2005) Isotopic fractionation of iron, potassium, and oxygen in stony cosmic spherules: Implications for heating histories and sources. *Geochim. Cosmochim. Acta* **69**, 2647–2662.

Tomeoka K., Kiriyama K., Nakamura K., Yamahana Y. and Sekine T. (2003). Interplanetary dust from the explosive dispersal of hydrated asteroids by impacts. *Nature* **423**, 60–62.

Toppani A., Libourel G., Engrand C. and Maurette M. (2001) Experimental simulation of atmospheric entry of micrometeorites. *Meteorit. Planet. Sci*. **36**, 1377–1396.

Van Ginneken, M., Folco L., Cordier C. and Rochette P. (2012) Chondritic micrometeorites from the Transantarctic Mountains, *Meteorit. Planet. Sci.* **47**, 228–247.

Vondrak T., Plane J. M. C., Broadley S. and Janches D. (2008) A chemical model of meteoric ablation. *Atmos. Chem. Phys.* **8**, 7015–7031.

Wasson J. T. and Rubin A. E. (2010) Metal in CR chondrites. *Geochim. Cosmochim. Acta* **74**, 2212–2230.

Weisberg M. K., Prinz M. and Nehru C. E. (1988) Petrology of ALH85085: A chondrite with unique characteristics. *Earth Planet. Sci. Lett.* **91**, 19–32.

Weisberg M. K., Prinz M., Clayton R. N., Mayeda T. K., Grady M. M., and Pillinger C. T. (1995) The CR chondrite clan. Proceedings of the Eighth Symposium on Antarctic Meteorites. pp. 11–32.

Yada T., Nakamura T., Takaoka N., Noguchi T., Terada K., Yano H., Nakazawa T. and Kojima H. (2004) The global accretion rate of extraterrestrial materials in the last glacial period estimated from the abundance of micrometeorites in Antarctic glacier ice. *Earth, Planets and Space* **56**, 67–79.

Yada T., Nakamura T., Noguchi T., Matsumoto N., Kusakabe M., Hiyagon H., Ushikubo T., Sugiura N., Kojima H., and Takaoka N. (2005) Oxygen isotopic and chemical compositions of cosmic spherules collected from the Antarctic ice sheet: Implications for their precursor. *Geochim. Cosmochim. Acta* **69**, 5789–5804.

Yiou F., Raisbeck G. M. and Brownlee D. (1985) ^{10}Be in Iron Type Cosmic Spherules: Evidence for a Differentiated Parent Body. *Meteoritics* **20**, 791–792.

FIGURE CAPTIONS

Figure 1

Back scattered electron images of S-type barred olivine spherules with Fe–Ni beads. AAS-38-167#1-P111 shows a large void space generated due to escape of volatiles during atmospheric entry. The particles generally have a magnetite rim on the edge. The Fe–Ni beads are situated mostly near the edge of the spherules and have sizes in the range of ~69–153 μm.

Figure 2

Back scattered electron images of G-type spherules with Fe–Ni beads. The dendritic magnetites are thinner in those spherules which contain a Fe-Ni bead. The beads are in the size range of ~47–140 μm with volume percent ranging from ~2–30 % of the spherule.

Figure 3

Back scattered electron images of I-type spherules with Fe–Ni beads. The spherules have different proportions of wustite and magnetite combination where the dark phases are magnetite while the light phases are wustite. The volumes of the beads are much larger than in the S- and G-type spherules. The beads are in the size range of ~44–214 μm.

Figure 4

Plot showing diameter of the spherules (μm) versus that of the Fe–Ni beads in the spherules (μm). The size of the beads increases with that of the spherule diameter indicating a correlation between them.

Figure 5

Co (wt%) versus Ni (wt%) plot of Fe–Ni beads in different types of cosmic spherules. The line labelled as chondritic line is the regression line for different types of chondrites. Many beads seems to fall close to the chondritic line, however there are some with high Ni and low Co content that have scattered on the upper left side of figure. The dotted elliptical shape defines the range close to chondritic line.

Figure 6

(a) Fe–Ni beads from the S-type spherules plotted with decreasing condensation temperatures of RMEs which are normalized to CI chondrite and Os values. The trend is more or less chondritic however, W and Mo show depletion. (b) CI normalized values of beads in S-type spherules for various PGE elemental ratios, all the beads seem to have chondritic values.

Figure 7

(a) Fe–Ni beads from the G-type spherules plotted with decreasing condensation temperatures of RMEs which are normalized to CI chondrite and Os values. The trend is in conformity with chondritic, however, W and Mo are depleted as seen in the beads of S-type spherules. (b) CI normalized values of beads in G-type spherules for various PGE elemental ratios, again all the values are close to chondritic values.

Figure 8

(a) G-type spherules without bead plotted with decreasing condensation temperatures of RMEs which are normalized to CI chondrite and Os values. The trend shows large variation and some are far from chondritic values. (b) CI normalized values of G-type spherules without beads for various PGE elemental ratios are having chondritic values.

Figure 9

(a) Fe–Ni beads from the I-type spherules plotted with decreasing condensation temperatures of RMEs which are normalized to CI chondrite and Os values. The trend is more or less chondritic, while W and Mo show depletion. (b) CI normalized values of beads in I-type spherules for various PGE elemental ratios have chondritic values. However, one of the beads is enriched in Os/Ir, Ru/Ir and Rh/Ir Pd/Ir ratio compared to others, this spherule possibly has a different type of parent body.

Figure 10

(a) I-type spherules without beads plotted with decreasing condensation temperatures of RMEs which are normalized to CI chondrite and Os values. The trend shows large variations similar to the G-type spherules. (b) CI normalized values of G-type spherules without bead for various PGE elemental ratios show large deviation from chondritic values. Even the most refractory elemental ratios of Os/Ir do not seem to be chondritic in many spherules.

Figure 11

The plot of Ni concentration (wt%) versus PGE data (ppm) in Fe–Ni beads from S-, G- and I-type cosmic spherules. There seems to be an increase in PGE concentration with the increase in Ni concentration.

Figure 12

The initial size of the dust particle estimated before it hit the earth's surface by segregating the concentration of PGE from different initial sizes into the beads of different sizes. The concentration of the PGE was assumed to have CI composition and homogenously distributed throughout the initial size of the dust. The concentration of the PGEs goes on increasing as the Fe–Ni bead size decreases and the initial size of the spherule increases. The bead in the process of forming nugget loses it Fe and Ni and pre-concentrates PGEs in a small size of <10 μm from a Fe–Ni bead size of ~50–300 μm.

Figure 13

Barred spherule with a Fe-rich region that contains a bead – both of which are in the process of being detached from the spherule AAS-26-D32-M-P1. This unique spherule has different textural features: the barred (lower half of spherule with large amount of magnetite), G-type (surrounding the bead) and the Fe–Ni bead at the edge of the spherule. The Fe content in G-type feature is more than that in barred portion, indicating mobility of metal towards the bead forming region.

Figure 14

Plots of Os versus Ir, Ru, Rh and Pd from Fe–Ni beads in all types of cosmic spherules. The solid line is the best fit line for all type of chondrites (Lodders and Fegley, 1998; Tagle and Berlin, 2008).

Figure 15

Plots of Rh and Pt versus Pd, Ru and Os versus Pt from Fe–Ni beads in all types of cosmic spherules. The solid line is the best fit line for all type of chondrites (Lodders and Fegley, 1998; Tagle and Berlin, 2008).

Figure 16

Plots of Re versus Os, Ir, Ru and Pt from Fe–Ni beads in all types of cosmic spherules. The solid line is the best fit line for all types of chondrites (Lodders and Fegley, 1998; Tagle and Berlin, 2008).

Figure 17

Histogram plot of various elemental ratios normalized to CI values for Fe–Ni beads of all types of cosmic spherules.

Fig. 1

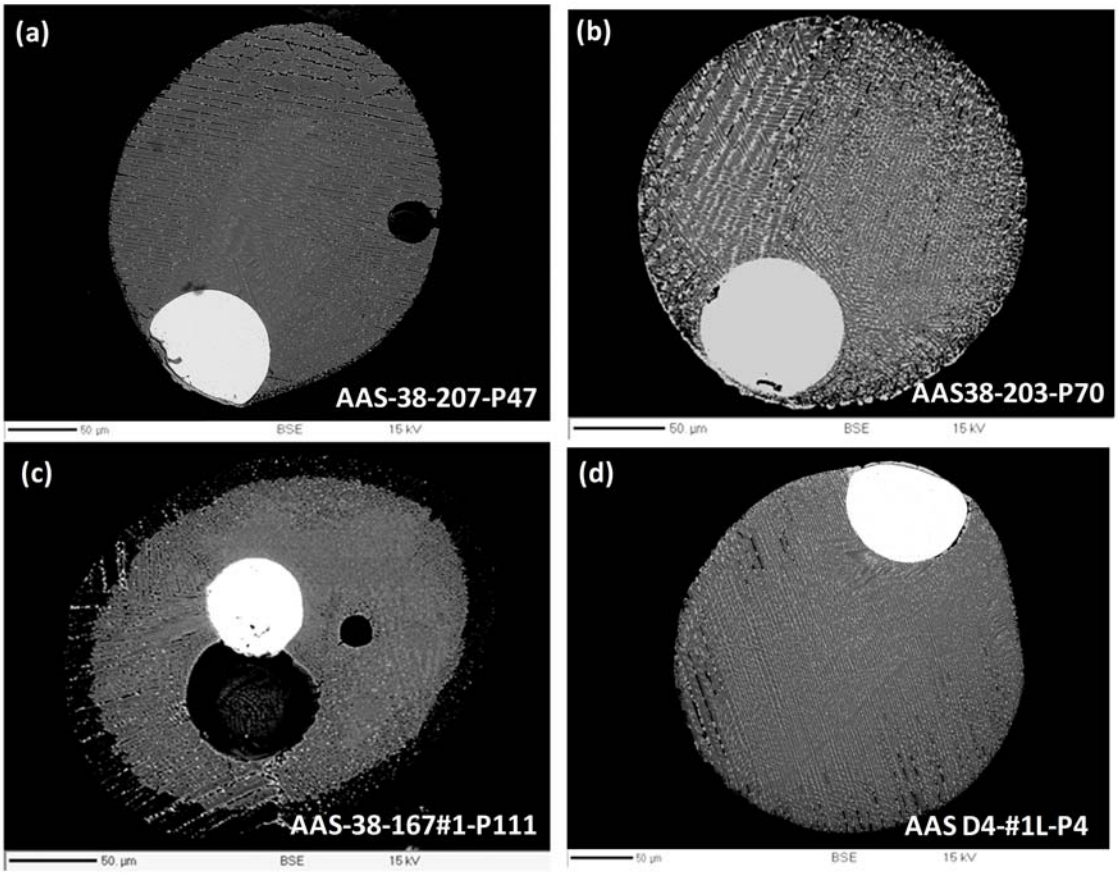
(a)
AAS-38-207-P47
50 µm BSE 15 kV
(b)
AAS38-203-P70
50 µm BSE 15 kV
(c)
AAS-38-167#1-P111
50 µm BSE 15 kV
(d)
AAS D4-#1L-P4
50 µm BSE 15 kV

Fig. 2

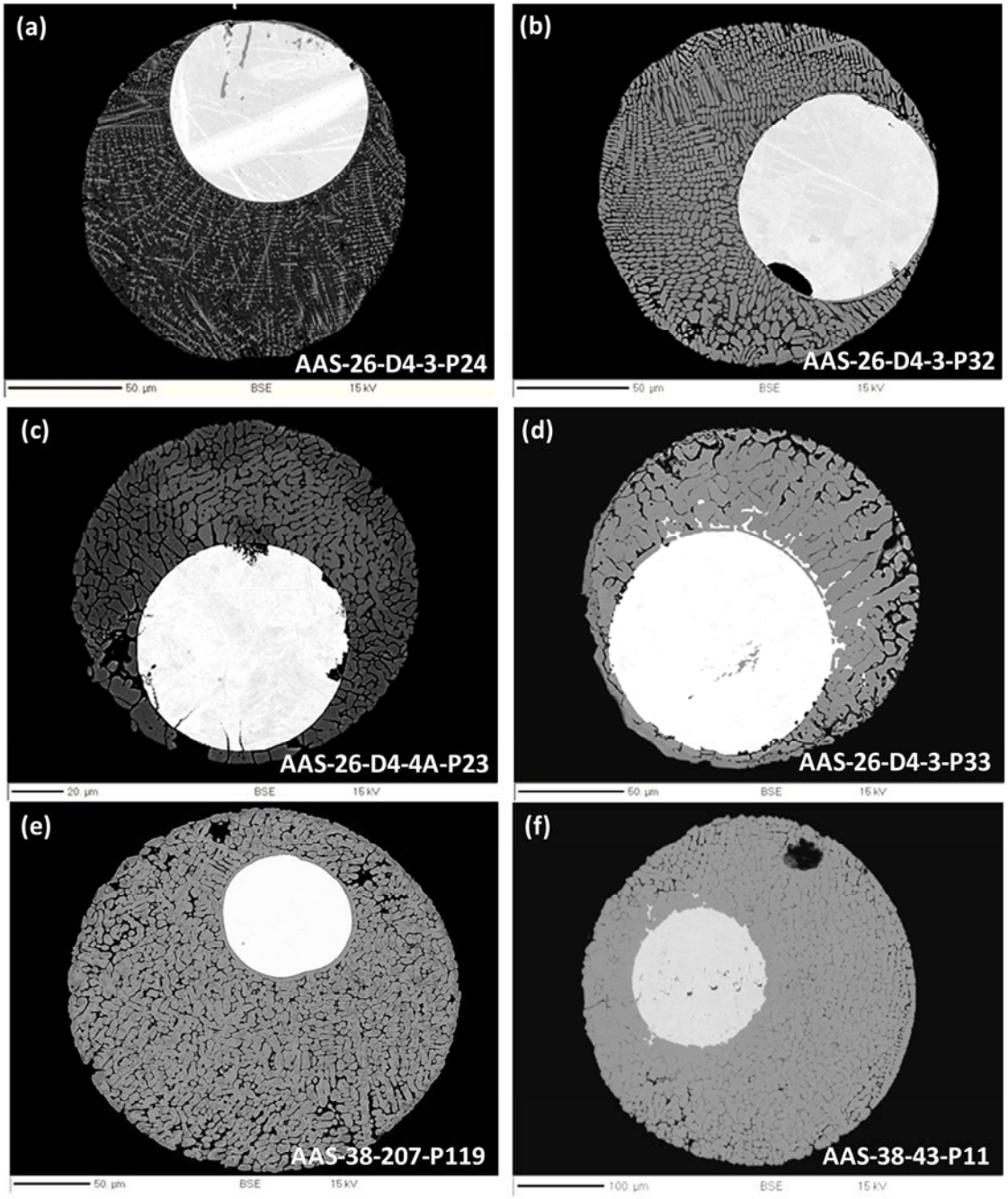
(a)
AAS-26-D4-3-P24
50 µm BSE 15 kV
(b)
AAS-26-D4-3-P32
50 µm BSE 15 kV
(c)
AAS-26-D4-4A-P23
20 µm BSE 15 kV
(d)
AAS-26-D4-3-P33
50 µm BSE 15 kV
(e)
AAS-38-207-P119
50 µm BSE 15 kV
(f)
AAS-38-43-P11
100 µm BSE 15 kV

Fig. 3

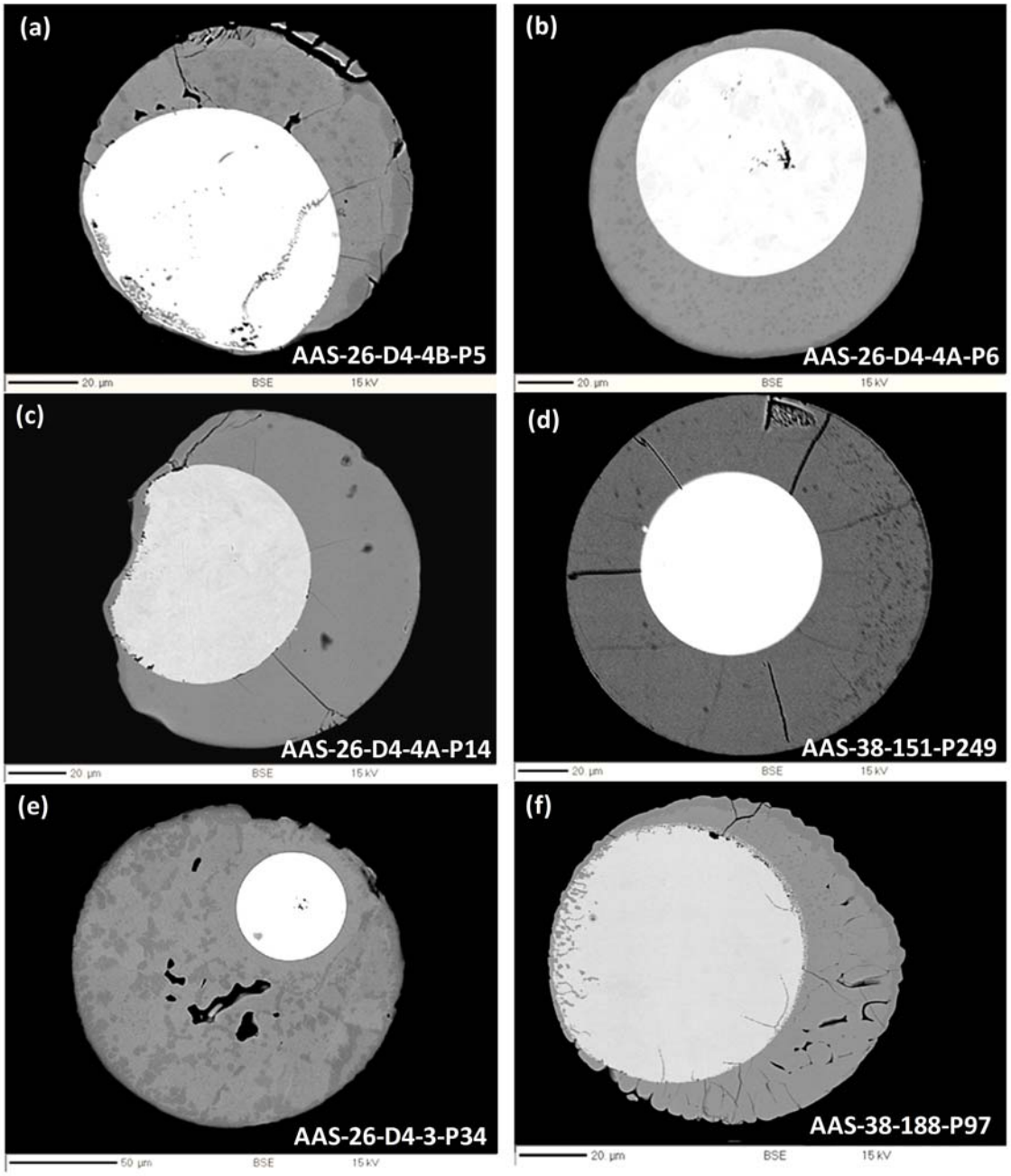
(a)
AAS-26-D4-4B-P5
20 µm BSE 15 kV
(b)
AAS-26-D4-4A-P6
20 µm BSE 15 kV
(c)
AAS-26-D4-4A-P14
20 µm BSE 15 kV
(d)
AAS-38-151-P249
20 µm BSE 15 kV
(e)
AAS-26-D4-3-P34
50 µm BSE 15 kV
(f)
AAS-38-188-P97
20 µm BSE 15 kV

Fig. 4

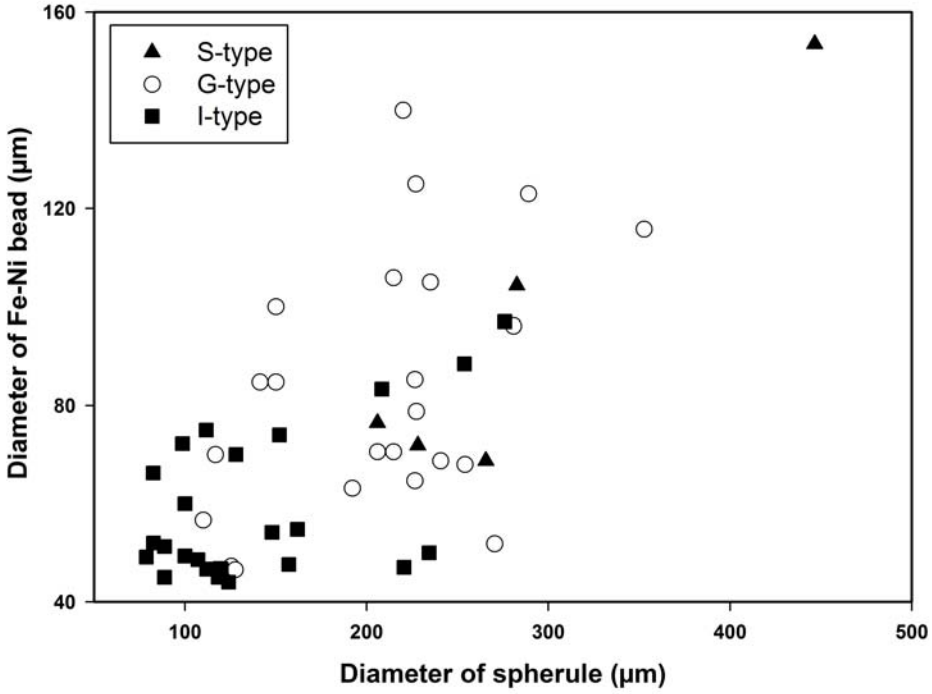
S-type
G-type
I-type
Diameter of Fe-Ni bead (μm)
Diameter of spherule (μm)
160
120
80
40
100
200
300
400
500

Fig. 5

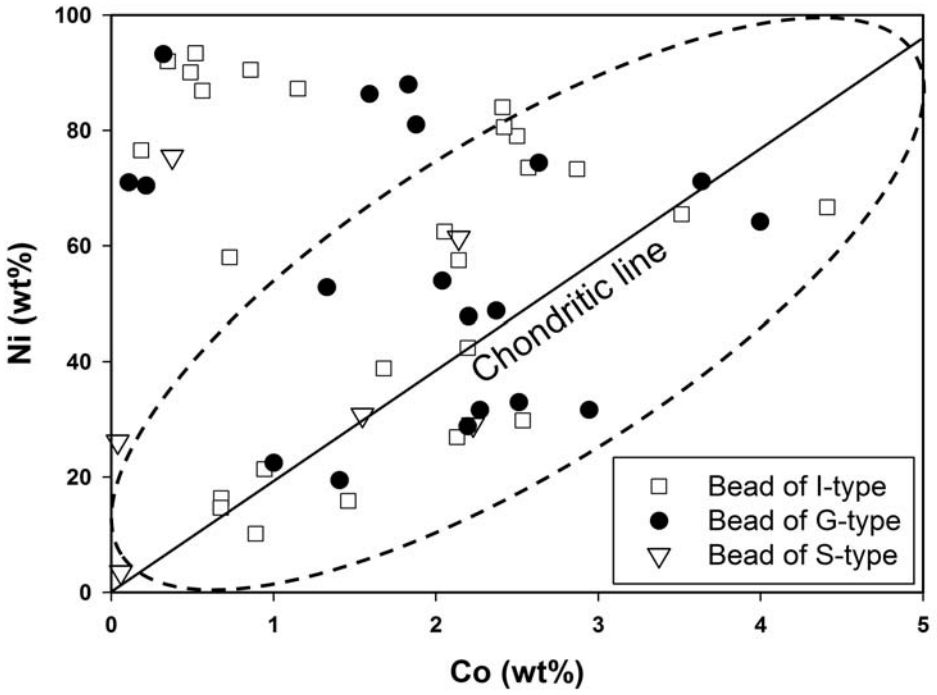
Chondritic line
Bead of I-type
Bead of G-type
Bead of S-type
Ni (wt%)
Co (wt%)
100
80
60
40
20
0
0
1
2
3
4
5

Fig. 6

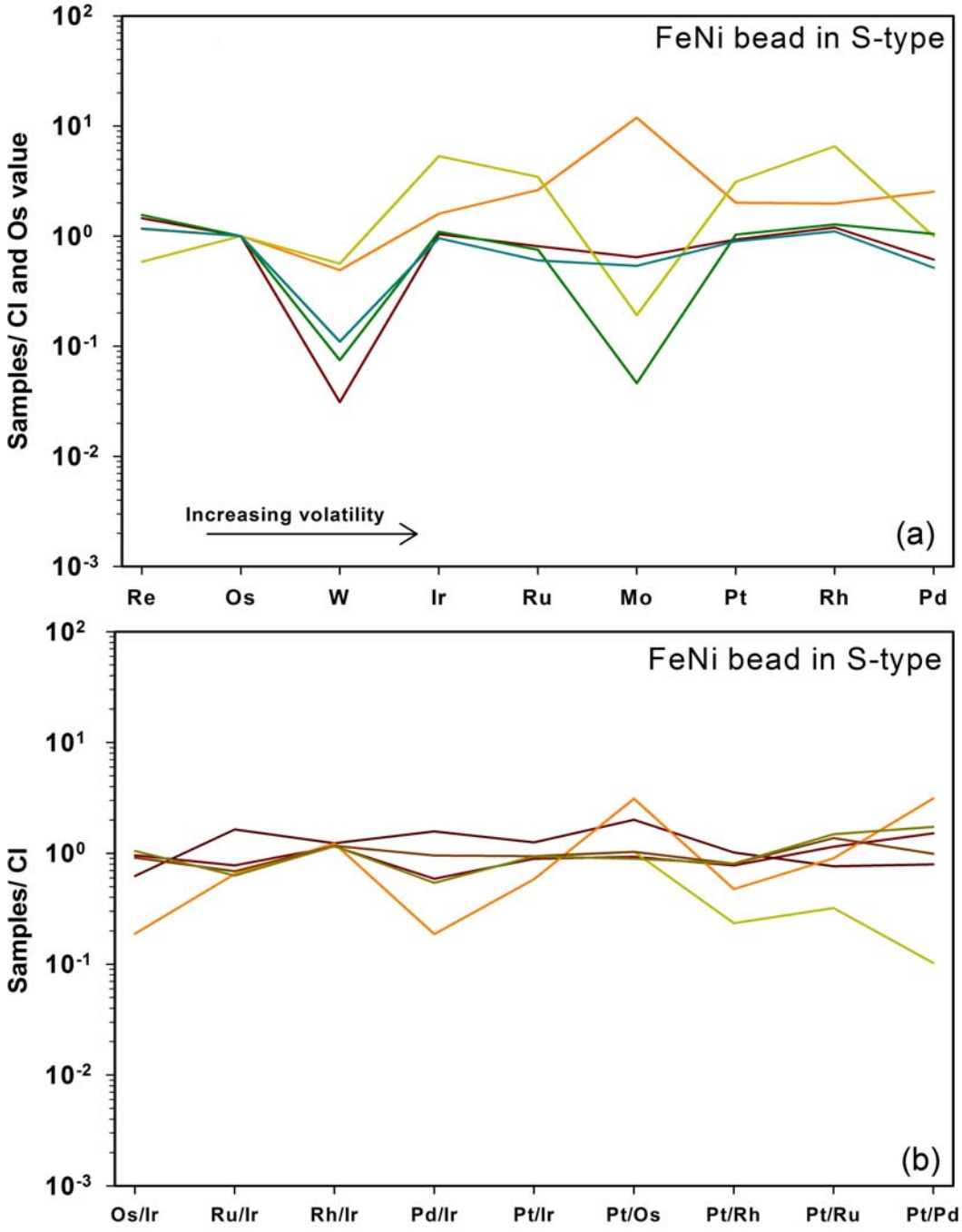
FeNi bead in S-type
Samples/ CI and Os value
10^2
10^1
10^0
10^{-1}
10^{-2}
10^{-3}
Increasing volatility
(a)
Re
Os
W
Ir
Ru
Mo
Pt
Rh
Pd
FeNi bead in S-type
Samples/ CI
(b)
Os/Ir
Ru/Ir
Rh/Ir
Pd/Ir
Pt/Ir
Pt/Os
Pt/Rh
Pt/Ru
Pt/Pd

Fig. 7

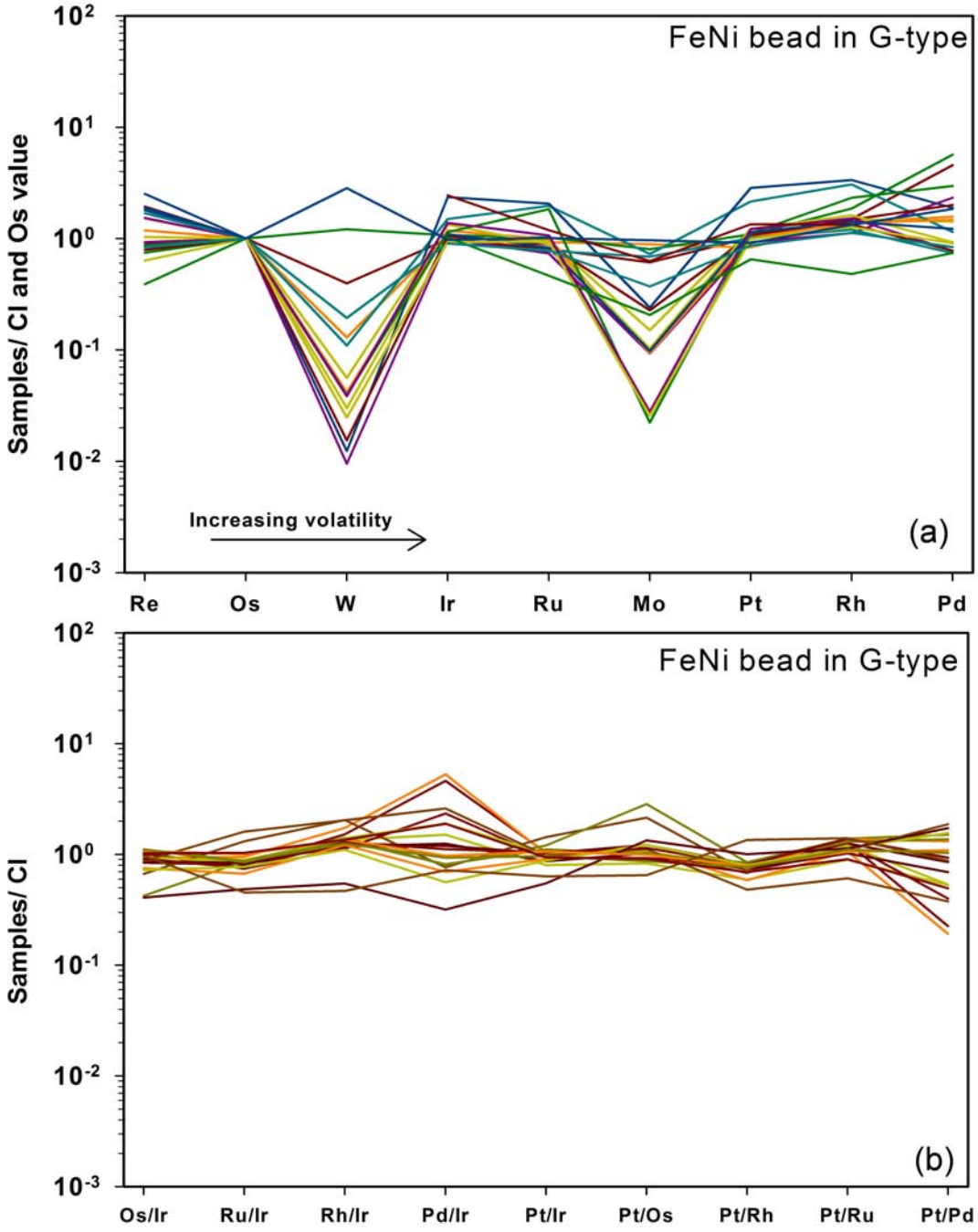
FeNi bead in G-type
Samples/ CI and Os value
10^2
10^1
10^0
10^{-1}
10^{-2}
10^{-3}
Increasing volatility
(a)
Re
Os
W
Ir
Ru
Mo
Pt
Rh
Pd
FeNi bead in G-type
Samples/ CI
(b)
Os/Ir
Ru/Ir
Rh/Ir
Pd/Ir
Pt/Ir
Pt/Os
Pt/Rh
Pt/Ru
Pt/Pd

Fig. 8

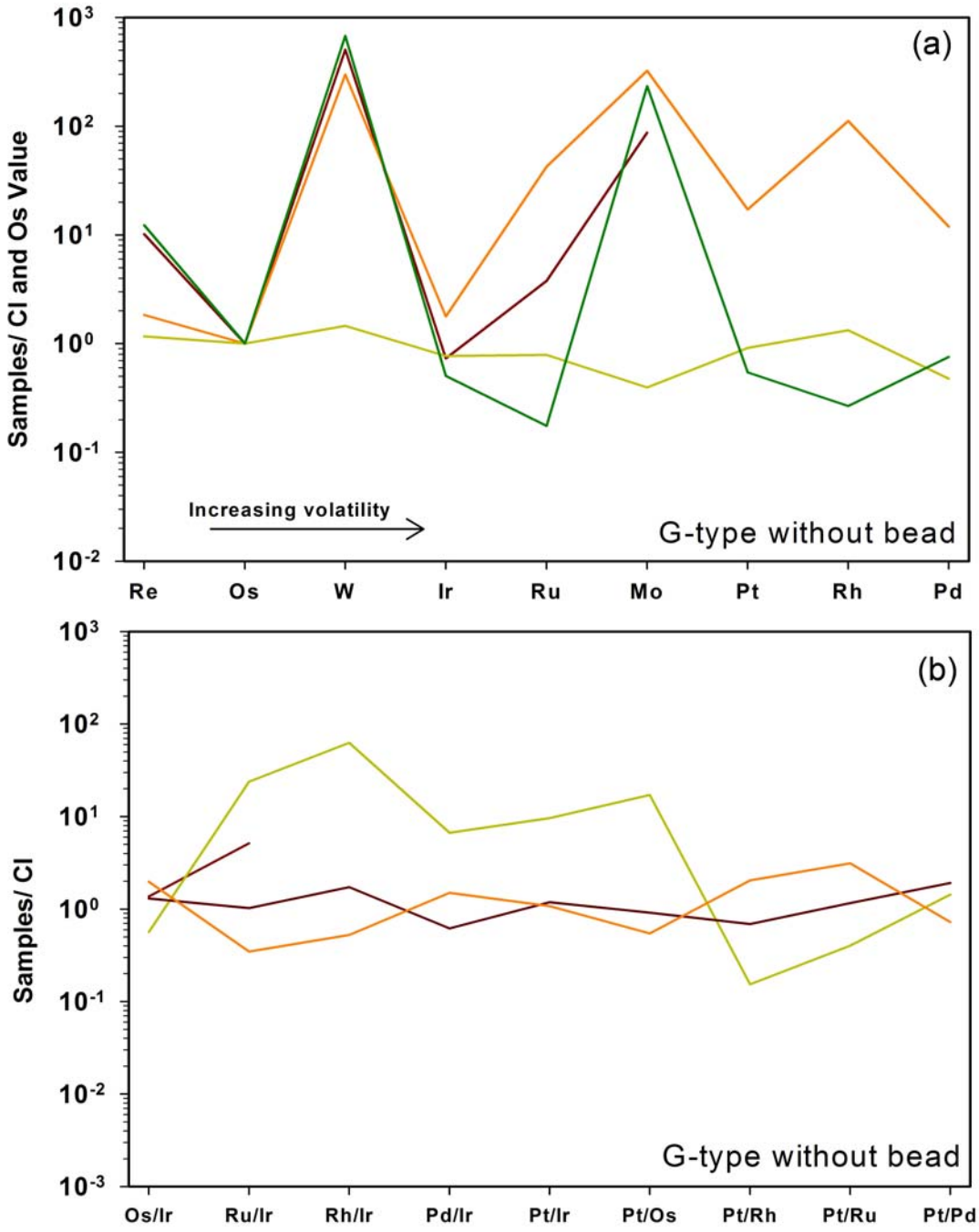
(a)
Samples/ Cl and Os Value
10^3
10^2
10^1
10^0
10^{-1}
10^{-2}
Increasing volatility
G-type without bead
Re
Os
W
Ir
Ru
Mo
Pt
Rh
Pd
(b)
Samples/ Cl
10^3
10^2
10^1
10^0
10^{-1}
10^{-2}
10^{-3}
G-type without bead
Os/Ir
Ru/Ir
Rh/Ir
Pd/Ir
Pt/Ir
Pt/Os
Pt/Rh
Pt/Ru
Pt/Pd

Fig. 9

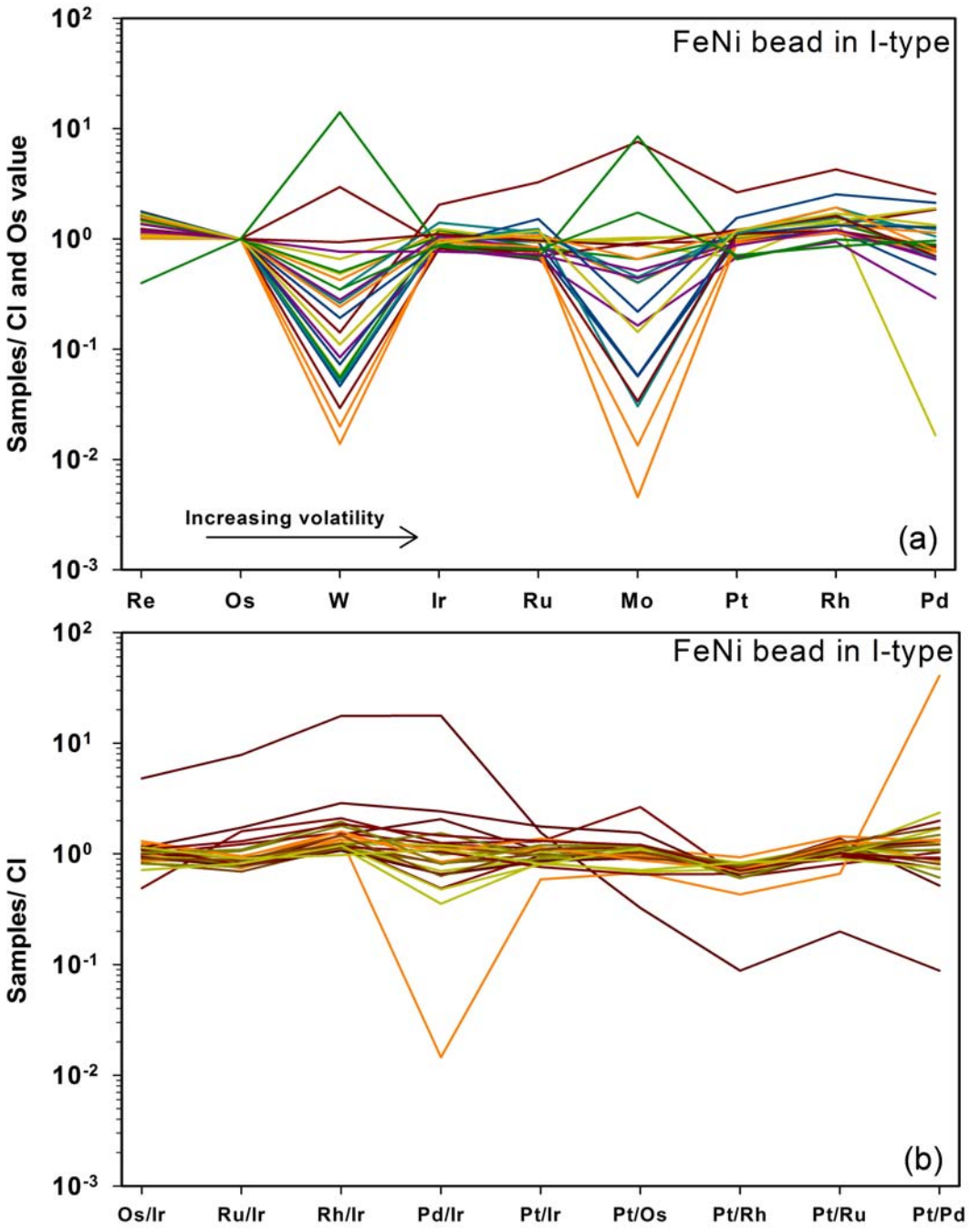
FeNi bead in I-type
Samples/ CI and Os value
Increasing volatility
(a)
Re
Os
W
Ir
Ru
Mo
Pt
Rh
Pd
FeNi bead in I-type
Samples/ CI
(b)
Os/Ir
Ru/Ir
Rh/Ir
Pd/Ir
Pt/Ir
Pt/Os
Pt/Rh
Pt/Ru
Pt/Pd

Fig. 10

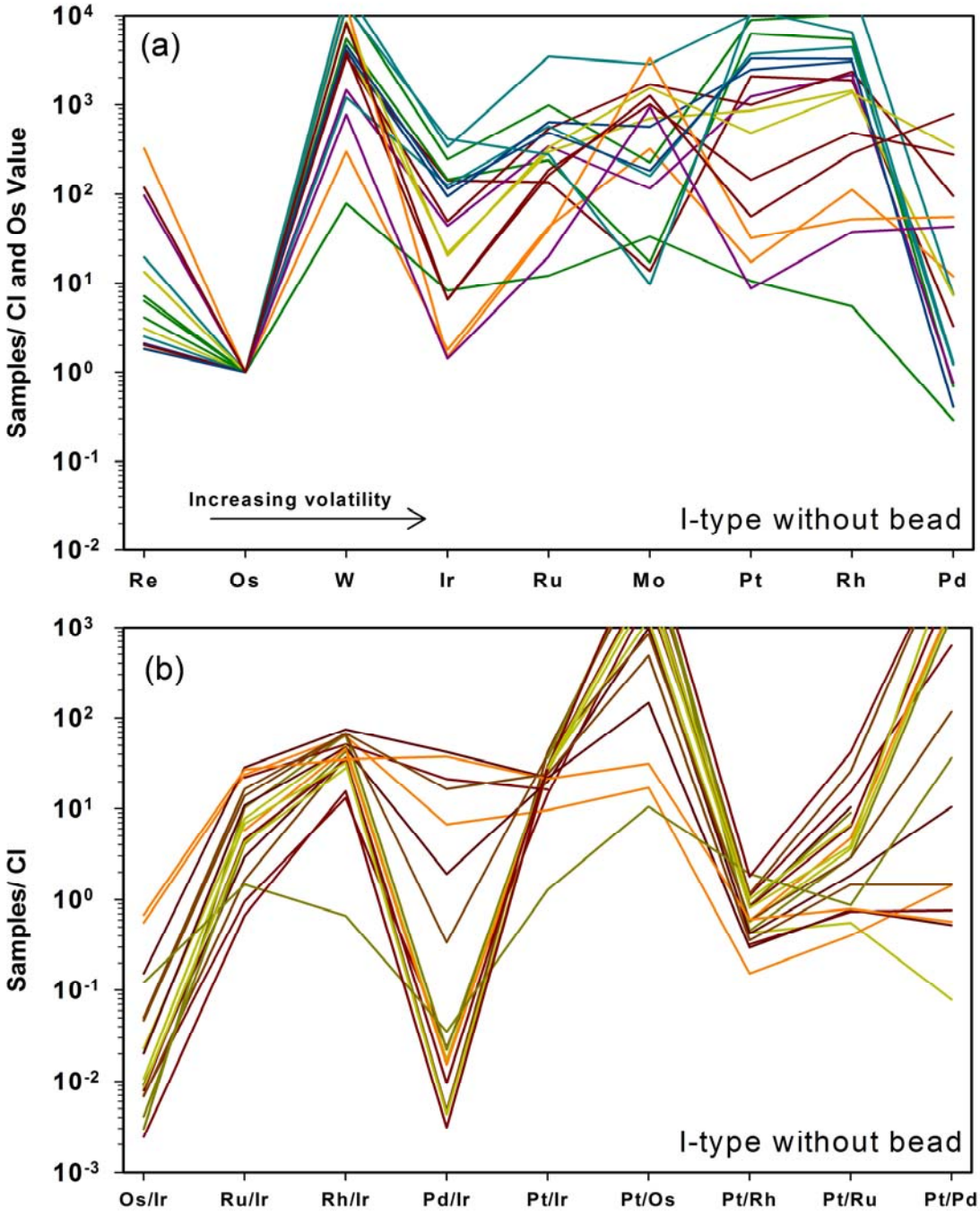
(a)
Samples/ CI and Os Value
10^4
10^3
10^2
10^1
10^0
10^{-1}
10^{-2}
Increasing volatility
I-type without bead
Re
Os
W
Ir
Ru
Mo
Pt
Rh
Pd
(b)
Samples/ CI
10^3
10^2
10^1
10^0
10^{-1}
10^{-2}
10^{-3}
I-type without bead
Os/Ir
Ru/Ir
Rh/Ir
Pd/Ir
Pt/Ir
Pt/Os
Pt/Rh
Pt/Ru
Pt/Pd

Fig. 11

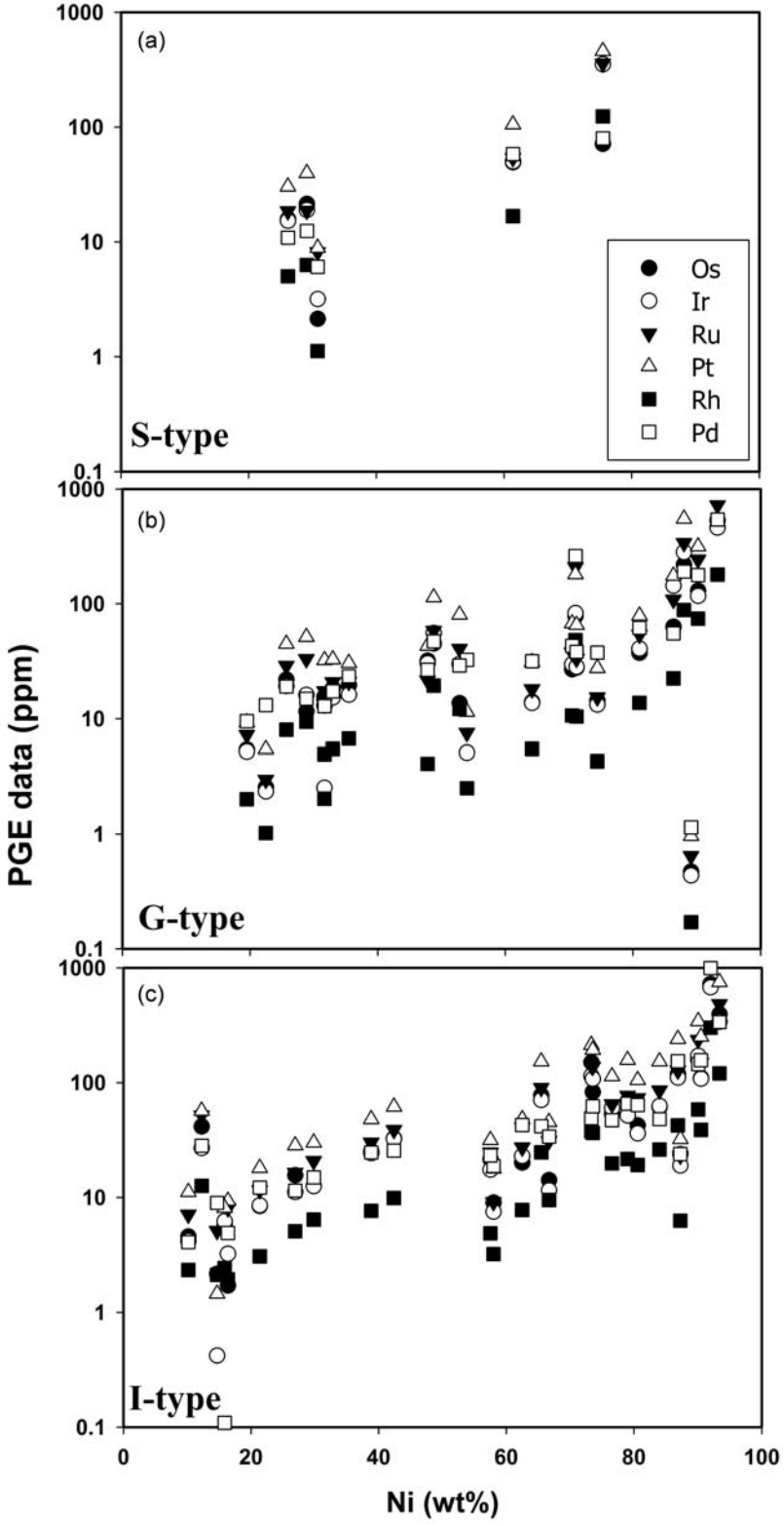
(a)
S-type
(b)
G-type
(c)
I-type
Os
Ir
Ru
Pt
Rh
Pd
PGE data (ppm)
Ni (wt%)
1000
100
10
1
0.1
0
20
40
60
80
100

Fig. 12

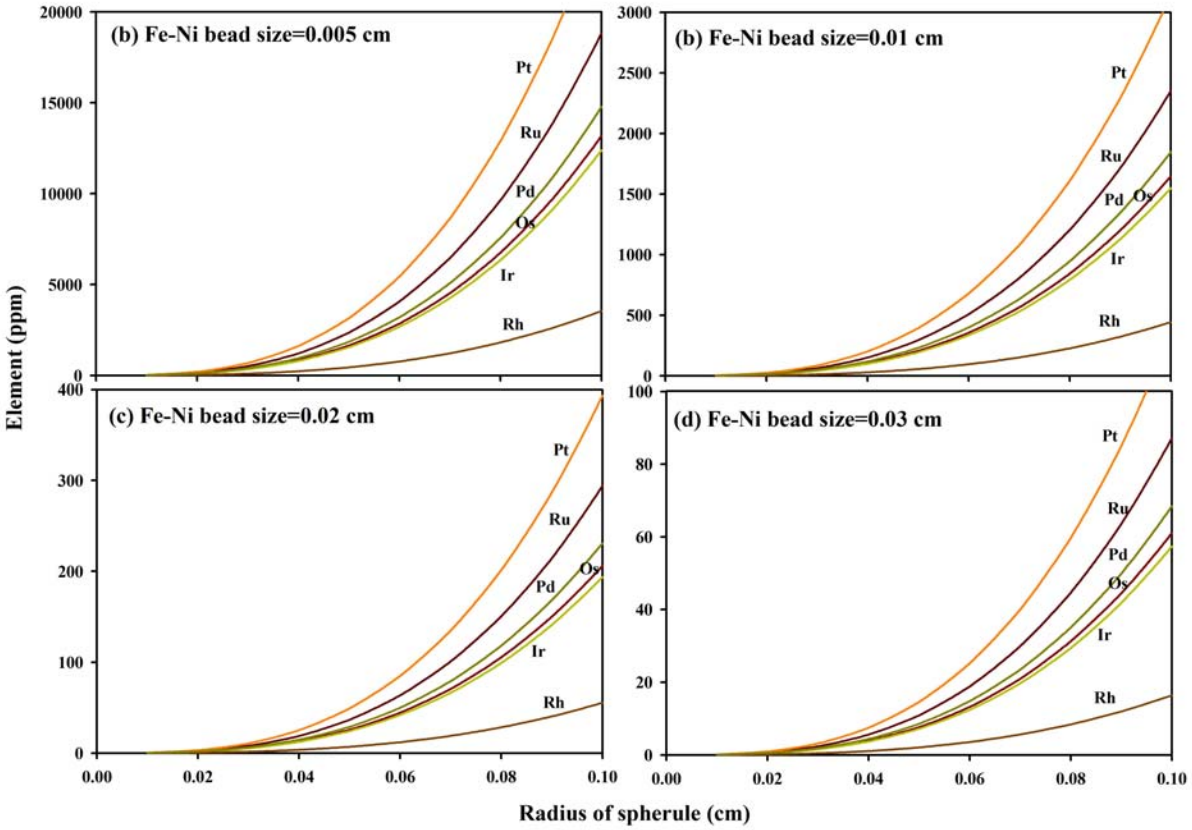
(b) Fe-Ni bead size=0.005 cm
(b) Fe-Ni bead size=0.01 cm
(c) Fe-Ni bead size=0.02 cm
(d) Fe-Ni bead size=0.03 cm
Pt
Ru
Pd
Os
Ir
Rh
Element (ppm)
Radius of spherule (cm)

Fig. 13

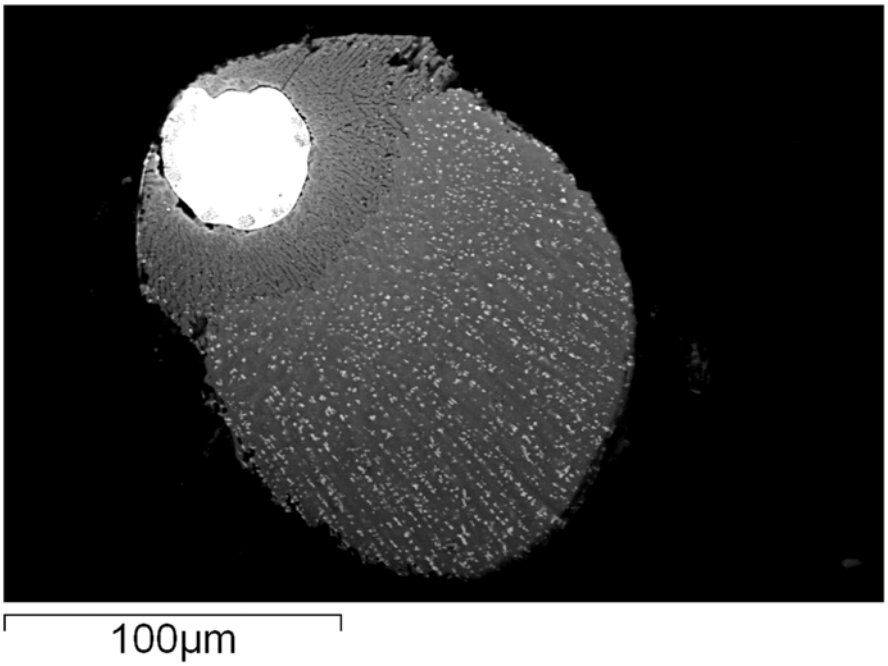
100μm

Fig. 14

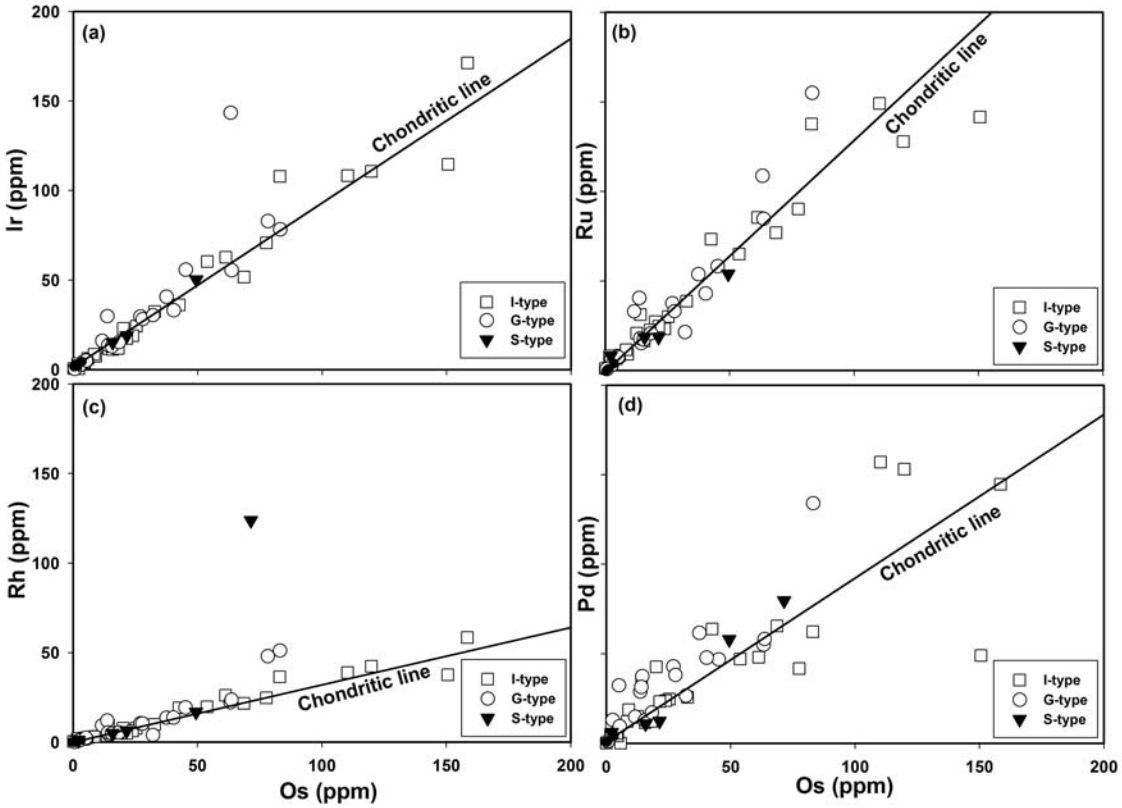
(a)
Ir (ppm)
Chondritic line
I-type
G-type
S-type
(b)
Ru (ppm)
Chondritic line
I-type
G-type
S-type
(c)
Rh (ppm)
Chondritic line
I-type
G-type
S-type
Os (ppm)
(d)
Pd (ppm)
Chondritic line
I-type
G-type
S-type
Os (ppm)
0
50
100
150
200

Fig. 15

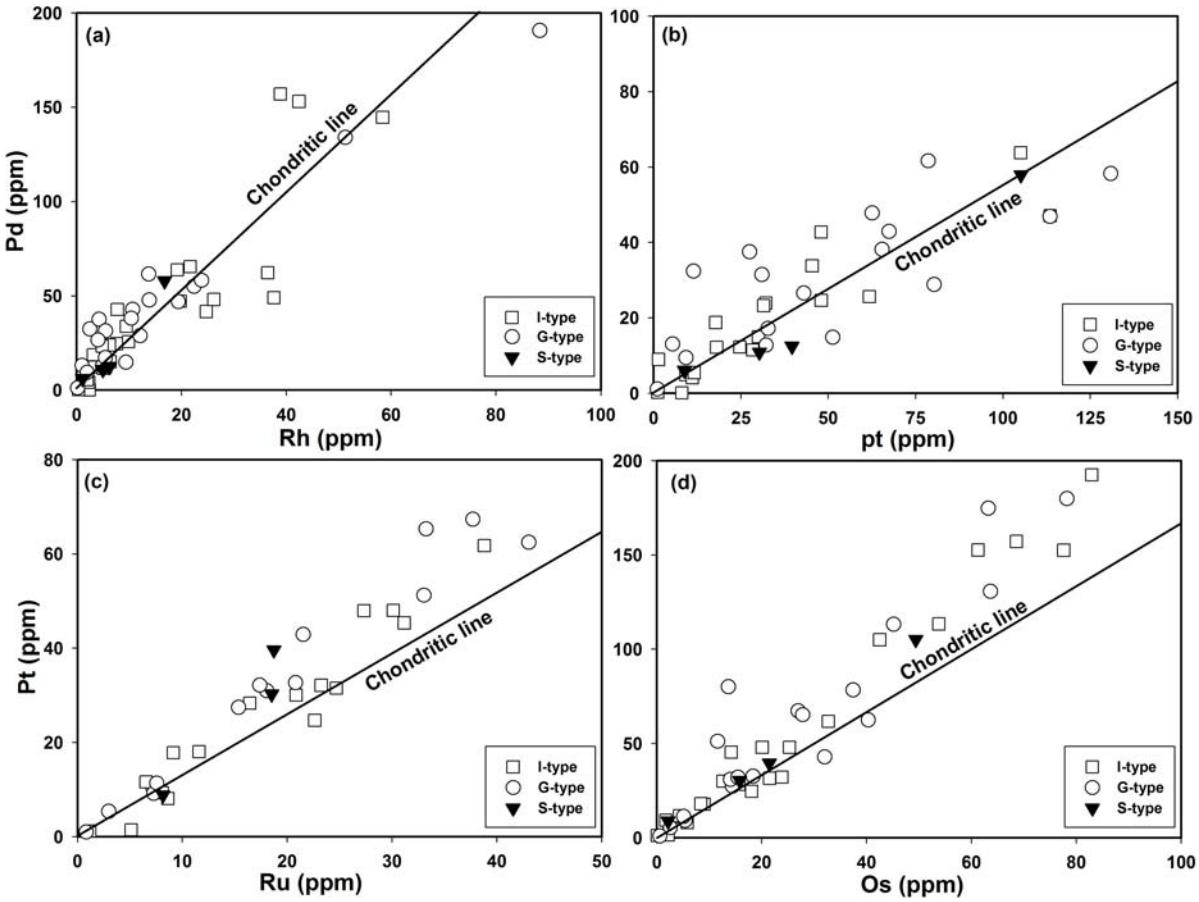
(a)
Pd (ppm)
Rh (ppm)
Chondritic line
I-type
G-type
S-type
(b)
pt (ppm)
Chondritic line
(c)
Pt (ppm)
Ru (ppm)
Chondritic line
(d)
Os (ppm)
Chondritic line

Fig. 16

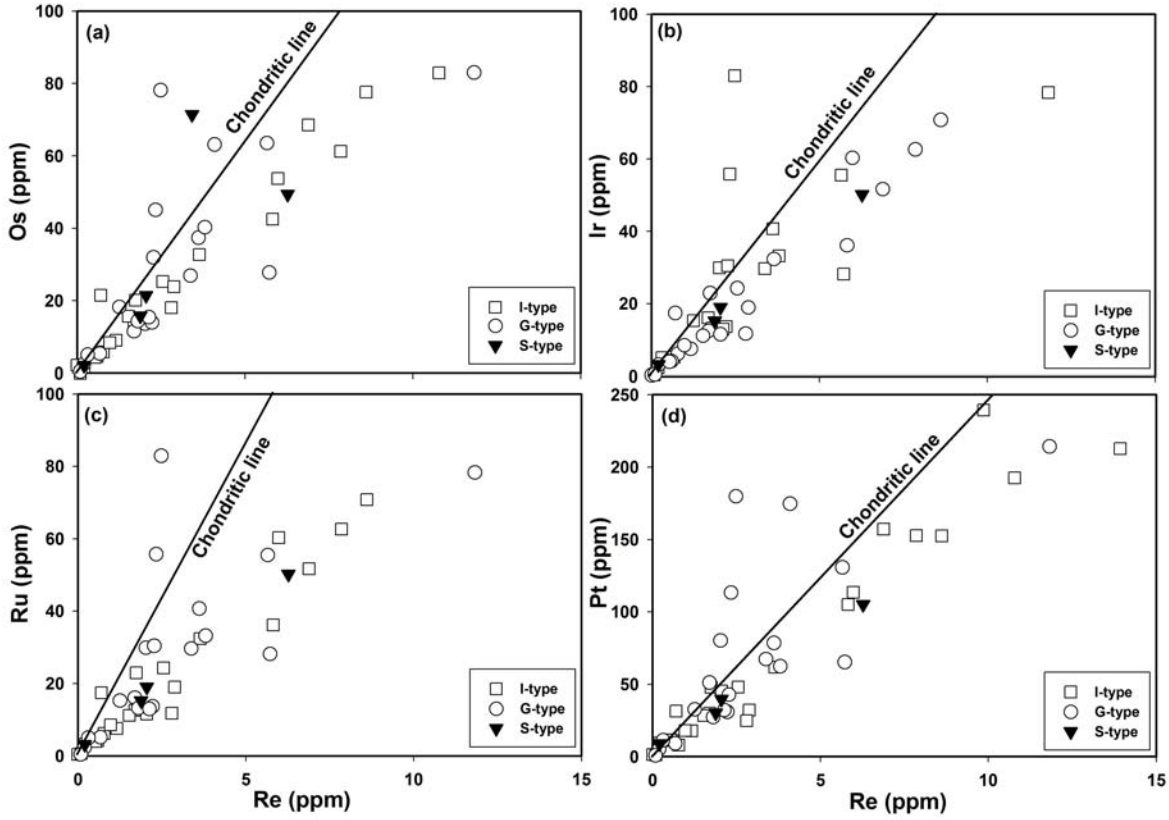
(a)
Os (ppm)
Chondritic line
I-type
G-type
S-type
(b)
Ir (ppm)
Chondritic line
I-type
G-type
S-type
(c)
Ru (ppm)
Chondritic line
I-type
G-type
S-type
Re (ppm)
(d)
Pt (ppm)
Chondritic line
I-type
G-type
S-type
Re (ppm)

Fig. 17

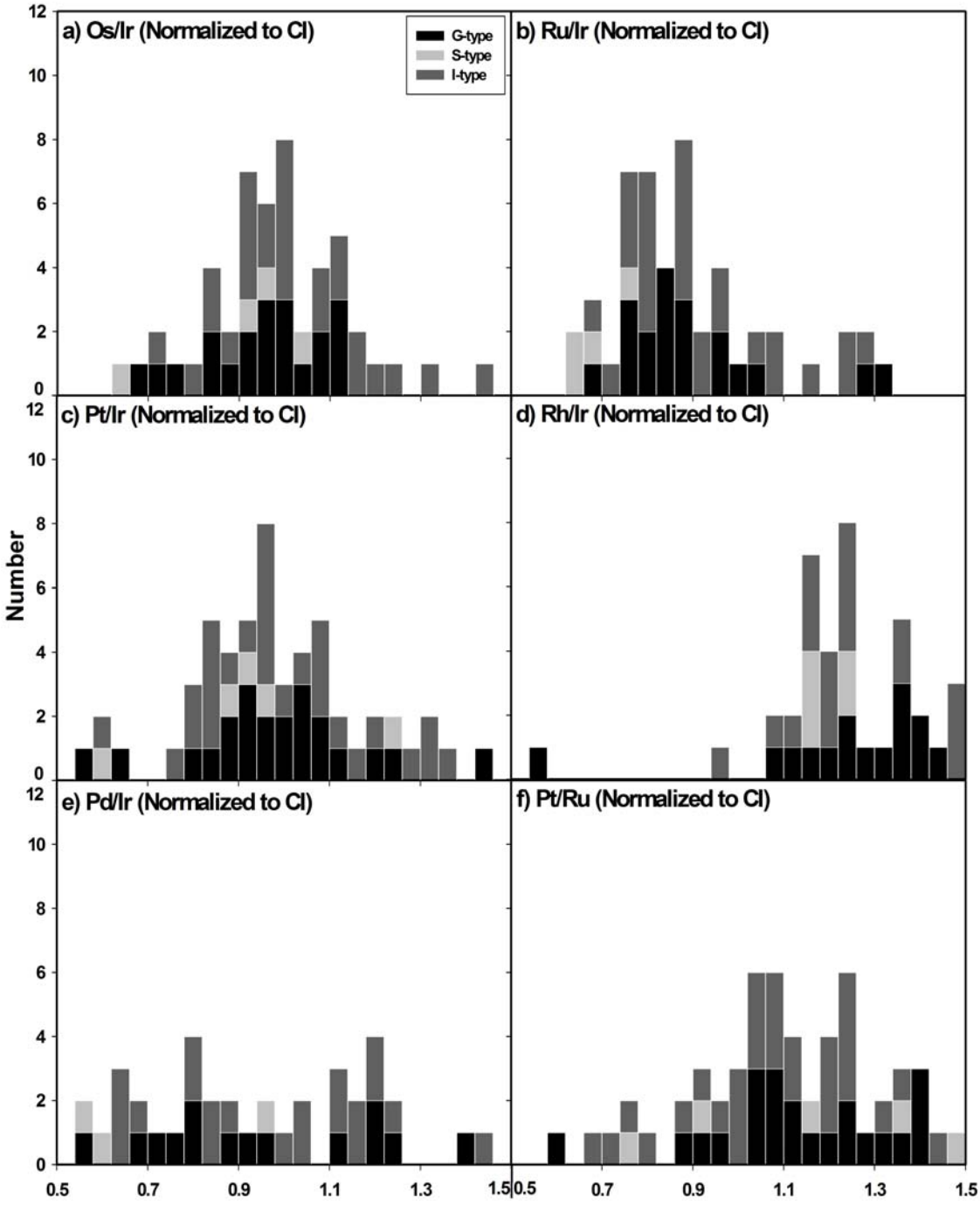
a) Os/Ir (Normalized to Cl)
b) Ru/Ir (Normalized to Cl)
c) Pt/Ir (Normalized to Cl)
d) Rh/Ir (Normalized to Cl)
e) Pd/Ir (Normalized to Cl)
f) Pt/Ru (Normalized to Cl)
G-type
S-type
I-type
Number
0
2
4
6
8
10
12
0.5
0.7
0.9
1.1
1.3
1.5

Table 1
The elemental compositions (wt%) of Fe–Ni bead and rest of the spherules obtained by defocused electron microprobe analyses.

Type	Sample Name	Size of Spherule (μm)	Size of Fe–Ni bead (μm)	% of bead volume	Fe–Ni bead				Rest of spherule						
					Fe	Co	Ni	Total	MgO	Al_2O_3	FeO	CoO	NiO	SiO_2	Total
S-type	AAS-D4-#1L-P4	447	153	4	73.9	–	26.2	100.0	15.3	1.3	50.8	–	–	29.8	97.2
	AAS-38-167-P111	266	69	2	67.3	1.5	30.8	99.7	25.5	0.9	34.4	0.1	0.7	38.2	101.8
	AAS-62-40-P17	228	72	3	23.8	0.4	75.5	99.8	21.0	2.1	40.4	0.3	2.3	31.7	100.1
	AAS-38-207-P47	283	104	5	39.2	2.1	61.4	102.8	25.4	1.9	34.5	–	0.1	36.7	100.3
	AAS-38-203-P70	206	76	5	69.6	2.2	29.1	101.0	16.7	2.2	48.7	–	0.1	30.9	100.9
G-type	AAS-26-D4-4A-P23	117	70	22	76.5	1.0	22.5	100.0	1.9	0.3	92.9	–	0.2	3.5	99.3
	AAS-26-D4-4A-P28	110	57	14	79.1	1.4	19.5	100.0	0.4	0.4	98.3	–	0.1	0.5	99.8
	AAS-26-D4-3-P24	141	85	22	29.2	0.2	70.5	99.9	16.6	1.2	55.8	–	0.4	27.1	101.9
	AAS-26-D4-3-P26	125	47	5	44.0	2.0	54.0	99.9	0.3	0.3	98.4	0.1	0.4	1.0	100.5
	AAS-26-D4-3-P32	150	85	18	69.0	2.2	28.8	99.7	2.8	1.2	88.0	0.1	0.1	8.3	100.8
	AAS-26-D4-3-P33	150	100	30	45.9	1.3	52.8	100.1	0.6	0.1	97.6	0.1	0.6	1.6	100.7
	AAS-38-173-P15	241	69	2	25.1	2.6	74.4	102.2	0.6	0.1	88.4	0.8	11.5	0.7	102.1
	AAS-38-151-P159	192	63	4	31.7	4.0	64.2	99.9	8.5	1.1	76.0	0.3	0.3	15.2	102.1
	AAS-38-206-P59	215	71	4	19.2	1.9	81.0	102.1	9.9	1.2	70.4	0.3	0.7	16.7	100.5
	AAS-62-61-P13	281	96	4	49.0	2.4	48.8	100.1	5.9	1.0	80.6	0.1	0.1	12.8	100.9
	AAS-62-61-P50	215	106	12	28.8	0.1	71.0	99.9	8.9	2.4	65.6	0.1	3.9	18.6	100.4
	AAS-62-40-P51	226	85	5	67.4	2.9	31.7	102.1	17.1	0.8	55.5	0.1	0.0	25.9	100.1
	AAS-62-40-P169	206	71	4	24.1	3.6	71.2	98.9	2.4	0.5	90.3	0.4	0.8	5.3	100.0
	AAS-38-187-P44	226	65	2	14.3	1.8	88.0	104.1	19.3	1.5	53.1	0.2	0.3	25.8	101.9
	AAS-38-207-P119	227	79	4	14.3	1.6	86.3	102.2	1.2	0.2	92.3	0.4	2.4	1.7	98.5
	AAS-38-188-P14	270	52	1	71.1	2.3	31.7	105.0	4.3	0.5	88.9	0.1	0.1	6.5	101.0
	AAS-38-188-P96	128	47	5	8.1	0.3	93.2	101.7	0.7	0.3	71.0	0.6	29.5	0.3	102.5
	AAS-38-204-P37	220	140	26	50.2	2.2	47.8	100.2	1.7	0.2	91.5	0.2	0.2	5.8	99.8
	AAS-38-43-P11	353	116	4	65.1	2.5	33.0	100.6	1.0	0.1	97.8	0.2	0.2	0.3	99.4
	AAS-26-D1#1-P4	235	105	9	9.4	1.4	89.1	99.9	16.1	0.6	55.9	0.8	2.1	23.4	99.0
	AAS-26-D3#1-P17	227	125	17	72.5	1.6	25.7	99.8	10.3	0.4	69.9	0.3	0.1	18.6	99.6

	AAS-26-D3#1-P20	254	68	2	9.5	0.5	90.2	100.3	13.0	1.1	58.8	0.7	1.7	24.3	99.7
	AAS-26-D1-I-P5	289	123	8	62.4	2.0	35.5	99.9	5.6	1.6	76.7	0.3	0.1	16.0	100.2
I-type	AAS-26-D4-4B-P5	83	66	52	82.9	0.7	16.4	100.0	–	–	96.7	0.1	1.2	–	98.1
	AAS-26-D4-4B-P7	118	45	5	9.5	0.5	90.1	100.0	–	–	92.2	0.4	6.3	–	99.0
	AAS-26-D4-4B-P10	89	51	19	83.1	0.7	14.7	98.5	0.1	0.2	97.1	–	0.5	0.4	98.4
	AAS-26-D4-4B-P11	79	49	24	82.7	1.5	15.9	100.0	0.2	0.1	97.5	0.2	1.9	0.3	100.1
	AAS-26-D4-4B-P20	117	47	6	22.9	0.2	76.5	99.6	–	–	93.6	0.1	6.4	0.1	100.1
	AAS-26-D4-4B-P29	89	45	13	67.6	2.5	29.8	100.0	0.2	0.2	98.6	0.1	0.5	0.3	99.9
	AAS-26-D4-4B-P33	124	44	4	31.0	3.5	65.5	100.0	–	–	96.0	0.3	0.8	–	97.2
	AAS-26-D4-4A-P3	148	54	5	23.8	2.9	73.3	100.0	–	–	98.9	0.5	1.7	0.1	101.2
	AAS-26-D4-4A-P6	112	75	30	41.2	0.7	58.0	99.9	–	–	99.8	0.1	0.7	–	100.7
	AAS-26-D4-4A-P9	128	70	16	12.5	0.6	86.9	99.9	–	–	95.8	0.2	4.3	–	100.4
	AAS-26-D4-4A-P14	100	60	22	77.6	0.9	21.4	99.9	0.6	–	99.7	–	0.1	0.8	101.3
	AAS-26-D4-4A-P19	83	52	25	59.5	1.7	38.8	100.1	0.1	–	99.1	0.1	0.4	0.2	99.9
	AAS-26-D4-3-P30	157	48	3	7.7	0.3	92.0	100.3	–	–	89.0	0.5	9.0	–	98.5
	AAS-26-D4-3-P34	162	55	4	8.7	0.9	90.5	100.1	–	–	92.8	0.5	5.2	–	98.5
	AAS-38-151-P249	152	74	12	55.3	2.2	42.4	99.9	0.1	–	98.8	0.1	0.4	0.1	99.4
	AAS-38-167-P66	254	88	4	21.3	2.5	79.0	102.8	–	–	96.6	0.4	1.7	0.1	98.8
	AAS-38-167-P101	234	50	1	6.6	0.5	93.4	100.6	0.1	0.1	89.3	0.7	9.1	0.1	99.5
	AAS-38-167-P106	208	83	6	37.3	2.1	62.5	101.8	–	–	98.5	0.1	0.7	–	99.4
	AAS-62-61-P51	221	47	1	12.4	1.2	87.2	100.8	0.1	–	99.2	0.3	1.0	0.2	100.9
	AAS-62-51-P105	100	49	12	24.8	2.6	73.5	100.9	0.1	–	99.2	0.3	1.0	0.2	100.9
	AAS-38-187-P61	120	47	6	31.6	4.4	66.7	102.6	0.2	0.1	99.7	0.2	0.4	0.3	100.9
	AAS-38-203-P138b	107	49	9	71.4	2.1	26.9	100.4	0.2	0.2	99.3	0.1	0.2	0.1	100.4
	AAS-38-188-P94	112	47	7	15.9	2.4	84.0	102.4	–	–	95.7	0.7	2.2	0.1	98.9
	AAS-38-188-P97	99	72	39	88.3	0.9	10.2	99.4	0.1	0.1	98.1	0.1	0.3	–	98.7
	AAS-38-204-P87	119	47	6	17.3	2.4	80.6	100.3	0.1	0.1	97.4	0.4	1.1	0.1	99.2
	AAS-38-43-P2	352	214	22	40.7	2.1	57.5	100.4	0.3	0.1	97.2	0.2	0.6	0.9	99.2
	AAS-26-D1-1-P9	276	97	4	86.9	0.5	12.3	99.6	–	–	93.2	0.6	6.0	–	99.8

Table 2
The RME compositions (ppm) of Fe–Ni bead for all different types of cosmic spherules. All errors are 1σ.

Type	Sample Name	Re	Os	W	Ir	Ru	Mo	Pt	Rh	Pd
S-type	AAS D4-#1L-P4	1.88 (0.16)	15.8 (1.2)	0.09 (0.03)	15.3 (0.7)	18.5 (1.1)	18.7 (1.6)	30.3 (2.1)	5.02 (0.54)	10.9 (0.9)
	AAS-38-167-P111	0.20 (0.09)	2.14 (1.49)	0.20 (0.14)	3.18 (1.54)	8.14 (3.59)	46.9 (11.9)	8.86 (4.35)	1.12 (0.58)	6.06 (3.12)
	AAS-62-40-P17	3.42 (0.34)	71.4 (5.7)	7.61 (0.84)	353 (25)	358 (32)	25.2 (3.1)	458 (24)	124 (11)	79.6 (12.1)
	AAS-38-207-P47	6.27 (0.69)	49.4 (5.1)	0.70 (0.23)	50.2 (3.9)	53.9 (7.8)	4.20 (0.65)	105 (8)	16.8 (2.5)	57.9 (15.2)
	AAS-38-203-P70	2.05 (0.24)	21.5 (3.3)	0.45 (0.07)	19.0 (1.6)	18.7 (1.8)	21.1 (3.7)	39.6 (3.1)	6.29 (0.83)	12.5 (2.1)
G-type	AAS-26-D4-4A-P23	0.19 (0.04)	2.56 (0.31)	0.19 (0.05)	2.35 (0.17)	2.97 (0.37)	2.87 (0.45)	5.41 (0.52)	1.02 (0.15)	13.1 (1.2)
	AAS-26-D4-4A-P28	0.67 (0.08)	5.40 (0.59)	0.13 (0.04)	5.20 (0.34)	7.25 (0.57)	8.82 (0.98)	9.24 (0.83)	2.01 (0.28)	9.49 (0.99)
	AAS 26-D4-3-P24	3.37 (0.68)	26.9 (5.7)	0.15 (0.05)	29.7 (4.9)	37.7 (7.1)	7.44 (1.03)	67.4 (11.7)	10.7 (1.7)	43.0 (3.7)
	AAS 26-D4-3-P26	0.31 (0.08)	5.09 (1.2)	1.17 (0.22)	5.07 (0.91)	7.5 (1.6)	7.48 (1.04)	11.4 (2.1)	2.51 (0.46)	32.4 (3.2)
	AAS 26-D4-3-P32	1.69 (0.27)	11.6 (2.1)	0.24 (0.05)	16.1 (2.1)	33.0 (4.9)	15.42 (1.53)	51.3 (7.1)	9.39 (1.26)	14.9 (1.1)
	AAS 26-D4-3-P33	2.02 (0.34)	13.7 (2.4)	0.03 (0.01)	29.9 (4.2)	40.6 (6.3)	5.99 (0.81)	80.2 (11.6)	12.1 (1.6)	28.9 (2.2)
	AAS-38-173-P15	1.80 (0.21)	14.4 (1.3)	0.03 (0.01)	13.3 (1.1)	15.4 (1.6)	2.46 (0.55)	27.5 (1.7)	4.27 (0.48)	37.6 (6.7)
	AAS-38-151-P159	2.22 (0.24)	14.0 (1.4)	0.04 (0.02)	13.7 (1.2)	18.0 (2.1)	5.84 (1.01)	31.0 (2.1)	5.49 (0.67)	31.5 (7.1)
	AAS-38-206-P59	3.61 (0.42)	37.4 (3.5)	0.30 (0.09)	40.7 (2.9)	53.8 (7.2)	6.46 (0.96)	78.6 (5.7)	13.7 (1.8)	61.7 (14.7)
	AAS-62-61-P13	2.33 (0.61)	45.1 (21.1)	0.48 (0.23)	55.8 (17.9)	58.3 (17.9)	8.52 (1.93)	113 (36)	19.4 (6.7)	47.0 (16.3)
	AAS-62-61-P50	2.48 (0.66)	78.2 (38.3)	0.58 (0.27)	83.0 (28.1)	208 (66)	3.19 (0.72)	180 (61)	48.1 (17.6)	261 (94)
	AAS-62-40-P51	2.13 (0.21)	15.5 (1.3)	0.57 (0.11)	13.1 (1.1)	17.4 (1.7)	19.52 (2.38)	32.2 (1.9)	4.93 (0.52)	12.8 (2.1)
	AAS-62-40-P169	5.72 (0.44)	27.8 (2.3)	–	28.2 (2.1)	33.2 (3.2)	4.99 (0.8)	65.4 (3.7)	10.4 (1.1)	38.1 (6.2)
	AAS-38-187-P44	16.3 (1.2)	219 (19)	1.60 (0.23)	281 (23)	338 (34)	11.19 (1.65)	549 (33)	88.3 (9.6)	191 (37)
	AAS-38-207-P119	4.09 (0.48)	63.2 (6.2)	0.12 (0.06)	143 (10)	109 (15)	72.74 (5.82)	175 (13)	22.4 (3.22)	55.1 (13.8)
	AAS-38-188-P14	–	–	324 (116)	2.53 (1.61)	13.3 (8.4)	882 (181)	–	2.03 (1.56)	–
	AAS-38-188-P96	44.9 (10.1)	532 (227)	2.49 (1.08)	461 (135)	722 (204)	25.1 (5.7)	1087 (321)	179 (57.5)	541 (173)
	AAS-38-204-P37	2.27 (0.27)	32.0 (4.7)	0.09 (0.05)	30.5 (2.4)	21.5 (2.01)	12.14 (2.18)	43.0 (3.1)	4.08 (0.53)	26.6 (4.0)
	AAS-38-43-P11	1.25 (0.16)	18.3 (2.6)	0.10 (0.03)	15.3 (1.2)	20.8 (1.8)	12.51 (2.15)	32.7 (2.4)	5.48 (0.67)	17.3 (2.5)
	AAS-26-D1#1-P4	0.08 (0.01)	0.47 (0.04)	0.11 (0.01)	0.44 (0.02)	0.65 (0.03)	0.36 (0.02)	0.96 (0.04)	0.17 (0.01)	1.14 (0.06)
	AAS-26-D3#1-P17	1.89 (0.46)	21.9 (1.4)	0.15 (0.02)	19.2 (0.6)	28.9 (1.2)	10.1 (0.6)	44.7 (1.7)	8.02 (0.81)	19.0 (1.4)

	AAS-26-D3#1-P20	14.1 (4.4)	130 (10)	5.84 (0.83)	117 (4)	243 (10)	20.4 (1.5)	315 (13)	74.2 (8.7)	177 (15)
	AAS-26-D1-I-P5	1.85 (0.24)	19.6 (1.1)	0.25 (0.02)	16.2 (0.7)	20.9 (0.9)	9.38 (0.79)	30.4 (1.1)	6.74 (0.28)	23.3 (1.3)
I-type	AAS 26-D4-4B-P5	0.21 (0.09)	1.71 (0.33)	0.05 (0.01)	3.24 (0.25)	8.08 (0.7)	23.9 (2.1)	9.32 (0.81)	1.94 (0.17)	4.91 (1.02)
	AAS 26-D4-4B-P7	23.1 (8.9)	158 (26)	12.7 (1.07)	171 (11)	235.7 (15.3)	116 (9)	343 (25)	58.4 (3.8)	145 (27)
	AAS 26-D4-4B-P10	–	2.17 (1.59)	26.9 (4.9)	0.42 (0.29)	5.13 (2.24)	589 (69)	1.45 (1.42)	2.12 (1.05)	8.97 (3.73)
	AAS 26-D4-4B-P11	0.78 (0.36)	5.83 (1.18)	0.06 (0.03)	6.22 (0.58)	8.62 (0.83)	9.49 (1.14)	8.11 (0.79)	2.43 (0.23)	0.11 (0.06)
	AAS 26-D4-4B-P20	5.98 (3.32)	53.8 (13.2)	0.56 (0.15)	60.3 (5.3)	65.0 (5.9)	65.0 (7.3)	114 (11)	19.8 (1.8)	47.1 (13.2)
	AAS 26-D4-4B-P29	1.70 (0.83)	12.6 (2.6)	0.63 (0.11)	12.6 (1.1)	20.8 (1.7)	10.4 (1.2)	30.0 (2.7)	6.43 (0.54)	15.0 (3.6)
	AAS 26-D4-4B-P33	8.61 (4.43)	77.6 (17.5)	0.68 (0.12)	70.8 (5.7)	90.2 (7.1)	8.09 (0.98)	153 (14)	24.8 (2.1)	41.7 (10.7)
	AAS-26-D4-4A-P3	13.9 (1.1)	151 (16.1)	2.40 (0.49)	115 (7)	142 (7)	45.4 (5.1)	213 (18)	37.6 (5.3)	49.1 (5.2)
	AAS-26-D4-4A-P6	1.16 (0.13)	9.03 (0.81)	5.06 (0.66)	7.54 (0.44)	9.13 (0.72)	15.3 (1.4)	17.8 (1.3)	3.22 (0.39)	18.8 (1.6)
	AAS-26-D4-4A-P9	9.86 (0.61)	120 (11)	0.32 (0.07)	111 (6)	128 (5.6)	2.95 (0.47)	240 (19)	42.4 (5.5)	153 (13)
	AAS-26-D4-4A-P14	0.97 (0.09)	8.43 (0.75)	0.77 (0.13)	8.56 (0.48)	11.6 (0.72)	15.9 (1.4)	18.1 (1.3)	3.07 (0.36)	12.2 (1.11)
	AAS-26-D4-4A-P19	2.55 (0.20)	25.3 (2.2)	2.41 (0.35)	24.3 (1.3)	30.1 (1.5)	23.9 (2.2)	48.0 (3.53)	7.68 (0.91)	24.7 (2.1)
	AAS 26-D4-3-P30	64.9 (11.6)	725 (144)	6.98 (1.05)	678 (105)	1295 (222)	40.5 (4.2)	1685 (272)	301 (46)	993 (75)
	AAS 26-D4-3-P34	14.6 (2.4)	110 (20)	1.52 (0.24)	108 (15)	149 (24)	11.6 (1.3)	251 (38)	38.9 (5.6)	157 (11)
	AAS-38-151-P249	3.64 (0.39)	32.7 (3.3)	1.74 (0.27)	32.4 (3.1)	38.8 (4.6)	30.8 (4.7)	61.8 (4.2)	9.90 (1.24)	25.7 (6.1)
	AAS-38-167-P66	6.88 (2.26)	68.6 (39.5)	0.38 (0.22)	51.7 (20.7)	77.0 (28.6)	4.24 (1.14)	157 (63.6)	21.7 (9.3)	65.4 (27.9)
	AAS-38-167-P101	35.4 (12.4)	395 (241)	1.49 (0.86)	340 (144)	483 (189)	3.30 (1.12)	751 (323)	120 (55)	337 (151)
	AAS-38-167-P106	1.74 (0.68)	20.1 (13.1)	2.50 (1.52)	22.9 (10.4)	27.3 (11.3)	36.4 (8.7)	47.9 (21.9)	7.80 (3.79)	42.7 (20.4)
	AAS-62-61-P51	2.88 (0.99)	23.9 (12.5)	63.7 (29.7)	19.0 (6.8)	23.2 (8.4)	373 (80)	32.1 (11.9)	6.28 (2.53)	23.9 (9.5)
	AAS-62-51-P105	10.8 (1.1)	83.0 (7.4)	5.48 (1.19)	108 (7)	138 (17)	61.4 (4.7)	193 (13)	36.5 (4.7)	62.3 (14.2)
	AAS-38-187-P61	2.05 (0.22)	14.2 (1.3)	0.52 (0.09)	11.6 (1.1)	31.2 (3.4)	5.72 (0.92)	45.4 (2.9)	9.53 (1.11)	33.8 (7.1)
	AAS-38-203-P138b	1.53 (0.23)	15.7 (2.6)	2.28 (0.27)	11.2 (1.2)	16.4 (1.8)	12.7 (2.6)	28.4 (2.4)	5.09 (0.74)	11.5 (2.1)
	AAS-38-188-P94	7.85 (2.81)	61.3 (27.3)	10.8 (5.1)	62.7 (18.6)	85.5 (28.1)	98.2 (26.6)	153 (46)	26.2 (9.1)	48.1 (18.6)
	AAS-38-188-P97	0.59 (0.16)	4.6 (2.1)	0.21 (0.11)	4.18 (1.29)	7.12 (2.16)	5.51 (1.22)	11.1 (3.4)	2.34 (0.81)	4.08 (1.41)
	AAS-38-204-P87	5.82 (0.67)	42.5 (6.5)	0.89 (0.17)	36.2 (3.1)	73.3 (6.6)	11.2 (2.3)	105 (7)	19.2 (2.4)	63.8 (9.8)
	AAS-38-43-P2	0.70 (0.14)	21.5 (3.1)	1.42 (0.23)	17.5 (1.4)	24.7 (2.4)	68.5 (10.6)	31.5 (2.4)	4.9 (0.6)	23.2 (3.51)
	AAS-26-D1-I-P9	6.44 (0.98)	41.6 (2.7)	2.43 (0.09)	27.0 (1.4)	52.0 (2.1)	12.7 (1.1)	56.7 (1.7)	12.6 (0.5)	28.2 (1.7)

Table 3
The RME compositions (ppm) of remaining region in some of Fe–Ni bead bearing cosmic spherules. All errors are 1σ.

Type	Sample Name	Re	Os	W	Ir	Ru	Mo	Pt	Rh	Pd
S-type	AAS D4-#1L-P4	–	–	0.01 (0.01)	–	–	0.01 (0.01)	–	–	–
	AAS-38-167-P111	–	–	–	–	–	0.01 (0.01)	–	–	–
	AAS-62-40-P17	–	–	–	–	–	–	–	–	–
	AAS-38-203-P70	–	–	0.01 (0.01)	–	–	0.01 (0.01)	–	–	–
G-type	AAS-26-D4-4A-P23	0.02 (0.01)	–	1.09 (0.11)	–	–	3.28 (0.34)	–	–	0.05 (0.03)
	AAS 26-D4-3-P24	0.01 (0.01)	–	1.07 (0.09)	–	–	8.58 (0.62)	–	0.01 (0.01)	0.09 (0.03)
	AAS 26-D4-3-P26	–	–	1.56 (0.11)	–	–	7.59 (0.54)	0.01 (0.01)	0.01 (0.01)	0.04 (0.01)
	AAS 26-D4-3-P32	0.01 (0.01)	–	2.05 (0.28)	–	–	4.99 (0.36)	0.02 (0.01)	0.01 (0.01)	0.02 (0.01)
	AAS 26-D4-3-P33	0.02 (0.01)	–	1.76 (0.17)	0.02 (0.01)	–	7.28 (0.56)	0.39 (0.02)	0.06 (0.01)	0.19 (0.02)
	AAS-26-D1#1-P4	0.01 (0.01)	0.08 (0.01)	2.12 (0.22)	0.06 (0.01)	0.25 (0.04)	5.80 (0.38)	0.11 (0.01)	0.04 (0.01)	0.18 (0.03)
	AAS-26-D3#1-P17	–	–	2.96 (0.33)	–	0.03 (0.02)	2.67 (0.22)	0.01 (0.01)	–	0.01 (0.01)
	AAS-26-D3#1-P20	–	–	1.09 (0.14)	–	0.09 (0.03)	3.76 (0.27)	–	0.01 (0.01)	–
	AAS-26-D1-I-P5	–	–	2.01 (0.08)	–	0.03 (0.01)	2.59 (0.23)	0.01 (0.01)	0.01 (0.01)	0.02 (0.01)
I-type	AAS-26-D4-4A-P3	0.28 (0.02)	–	0.12 (0.01)	0.38 (0.21)	–	1.51 (0.11)	3.05 (0.17)	0.43 (0.01)	0.70 (0.15)
	AAS-26-D4-4A-P9	0.02 (0.01)	–	3.77 (0.25)	–	–	26.3 (1.8)	0.05 (0.01)	–	0.09 (0.03)
	AAS 26-D4-3-P30	0.04 (0.01)	–	3.39 (0.19)	–	–	13.2 (0.7)	0.09 (0.02)	0.02 (0.01)	0.41 (0.09)
	AAS 26-D4-3-P34	0.04 (0.01)	–	3.28 (0.22)	0.02 (0.01)	–	16.9 (1.3)	0.22 (0.03)	0.05 (0.01)	0.27 (0.05)
	AAS-26-D1-I-P9	0.02 (0.01)	0.01 (0.01)	3.10 (0.12)	–	0.04 (0.02)	16.8 (1.4)	0.03 (0.01)	0.01 (0.01)	0.17 (0.03)

Table 4
The RME compositions (ppm) in non-bead cosmic spherules. All errors are 1σ.

Type	Sample Name	Re	Os	W	Ir	Ru	Mo	Pt	Rh	Pd
G-type	AAS-26-D1#3-P12	–	0.01 (0.01)	0.51 (0.21)	–	0.03 (0.01)	0.85 (0.24)	–	–	0.01 (0.01)
	AAS-26-D1#1-P7	–	0.01 (0.01)	0.45 (0.05)	0.01 (0.01)	0.49 (0.07)	4.74 (0.36)	0.28 (0.03)	0.24 (0.02)	0.11 (0.02)
	AAS-26-D6-P6	0.04 (0.01)	0.42 (0.16)	0.12 (0.06)	0.30 (0.12)	0.48 (0.11)	0.31 (0.09)	0.79 (0.28)	0.15 (0.03)	0.22 (0.02)
	AAS-26-D3#1-P2	0.02 (0.01)	0.02 (0.01)	3.08 (2.07)	0.01 (0.0)	0.01 (0.01)	10.3 (5.1)	0.03 (0.02)	–	0.02 (0.01)
I-type	AAS-26-D1#1-P1	–	0.01 (0.01)	6.74 (0.62)	1.39 (0.08)	2.07 (0.15)	0.26 (0.04)	45.0 (1.5)	5.23 (0.23)	0.04 (0.01)
	AAS-26-D1#1-P2	0.01 (0.01)	–	3.76 (0.36)	–	0.05 (0.01)	14.5 (0.8)	0.04 (0.01)	0.01 (0.01)	0.27 (0.04)
	AAS-26-D1#1-P6	–	0.01 (0.01)	4.52 (0.49)	0.81 (0.05)	3.71 (0.25)	1.81 (0.15)	54.9 (1.9)	8.55 (0.39)	–
	AAS-26-D1#1-P8	0.01 (0.01)	–	1.41 (0.17)	–	0.24 (0.06)	5.74 (0.44)	0.15 (0.02)	0.14 (0.01)	1.60 (0.14)
	AAS-26-D1#1-P9*	–	0.01 (0.01)	7.63 (0.96)	1.01 (0.07)	2.57 (0.21)	0.23 (0.04)	95.0 (3.5)	10.54 (0.52)	0.01 (0.01)
	AAS-26-D1#1-P10	–	1.46 (0.75)	0.99 (0.54)	8.99 (1.25)	7.44 (4.23)	2.76 (1.61)	–	0.49 (0.28)	0.83 (0.81)
	AAS-26-D1#3-P1	–	–	0.03 (0.01)	–	–	0.01 (0.01)	–	–	0.01 (0.01)
	AAS-26-D1#3-P3	–	–	4.36 (0.15)	0.38 (0.02)	6.00 (0.28)	6.26 (0.39)	24.8 (1.3)	6.98 (0.26)	0.01 (0.01)
	AAS-26-D1#3-P5	–	–	2.17 (0.08)	0.05 (0.01)	1.83 (0.12)	6.66 (0.43)	1.92 (0.12)	0.77 (0.03)	1.37 (0.15)
	AAS-26-D1#3-P8	–	0.01 (0.01)	2.58 (0.09)	0.38 (0.02)	4.61 (0.26)	1.98 (0.16)	23.5 (1.4)	5.33 (0.21)	0.01 (0.01)
	AAS-26-D1#3-P9	–	–	2.26 (0.08)	0.16 (0.01)	2.65 (0.17)	10.5 (0.7)	6.96 (0.46)	2.10 (0.09)	0.36 (0.05)
	AAS-26-D1#3-P10	0.01 (0.01)	–	5.57 (0.2)	0.61 (0.04)	5.52 (0.32)	7.2 (0.56)	36.9 (2.5)	8.05 (0.32)	0.01 (0.01)
	AAS-26-D1#3-P11	–	0.01 (0.01)	9.03 (3.64)	0.20 (0.06)	4.38 (0.59)	13.2 (3.6)	17.9 (4.4)	3.88 (0.76)	0.08 (0.02)
	AAS-26-D1#3-P13	–	–	8.55 (3.64)	0.75 (0.22)	4.69 (0.65)	1.37 (0.42)	60.6 (15.8)	9.08 (1.87)	–
	AAS-26-D1#3-P15	0.01 (0.01)	0.21 (0.07)	3.19 (1.48)	0.09 (0.02)	0.06 (0.02)	25.9 (8.2)	0.03 (0.01)	–	0.02 (0.01)
	AAS-26-D1#3-P17	–	0.01 (0.01)	2.67 (1.36)	1.37 (0.48)	9.75 (1.57)	3.44 (1.21)	88.7 (27.3)	13.6 (3.3)	0.02 (0.01)
	AAS-26-D1#3-P18	–	0.01 (0.01)	5.86 (3.15)	0.67 (0.23)	7.12 (1.22)	8.03 (2.97)	39.1 (12.6)	6.21 (1.59)	–
	AAS26-D1#3-P20	–	–	1.97 (1.23)	0.04 (0.01)	1.13 (0.24)	15.0 (6.4)	0.39 (0.15)	0.48 (0.15)	0.13 (0.02)
	AAS-26-D1#3-P21	–	0.01 (0.01)	4.42 (2.89)	0.04 (0.01)	1.66 (0.35)	11.3 (5.1)	1.83 (0.71)	0.79 (0.24)	1.89 (0.12)
	AAS-26-D6-P1	0.06 (0.01)	–	5.48 (2.41)	–	0.13 (0.03)	13.3 (3.3)	0.14 (0.04)	0.03 (0.01)	0.14 (0.02)
	AAS-26-D6-P2	–	–	5.72 (2.57)	0.07 (0.02)	1.68 (0.34)	9.87 (2.52)	3.50 (1.11)	1.26 (0.27)	1.30 (0.13)
	AAS-26-D6-P3	0.12 (0.03)	0.35 (0.13)	5.18 (2.41)	2.68 (0.93)	6.12 (1.25)	21.2 (5.5)	7.60 (2.49)	0.51 (0.11)	0.11 (0.02)
	AAS-26-D6-P5	–	0.01 (0.01)	20.1 (10.1)	3.22 (1.19)	3.37 (0.73)	0.15 (0.05)	201 (69)	14.4 (3.4)	0.01 (0.01)

AAS-26-D6-P7*	–	0.01 (0.01)	11.7 (6.4)	1.44 (0.58)	9.53 (2.19)	4.54 (1.42)	91.0 (34.8)	11.6 (2.9)	–
AAS-26-D6-P8	0.09 (0.02)	0.01 (0.01)	1.60 (0.92)	0.01 (0.01)	0.31 (0.09)	18.6 (6.2)	0.19 (0.08)	0.11 (0.03)	0.52 (0.07)
AAS-26-D6-P13	0.03 (0.01)	–	5.13 (3.43)	0.02 (0.01)	0.78 (0.21)	7.65 (2.88)	0.38 (0.17)	0.25 (0.08)	2.92 (0.37)
AAS-26-D3#1-P4	0.17 (0.11)	–	3.28 (2.35)	–	0.08 (0.02)	11.8 (6.3)	0.06 (0.04)	0.02 (0.01)	0.20 (0.02)
AAS-26-D3#1-P5	0.13 (0.08)	–	5.66 (4.25)	0.02 (0.01)	0.27 (0.07)	25.3 (14.2)	0.30 (0.19)	0.13 (0.05)	1.49 (0.12)
AAS-26-D3#1-P6	0.01 (0.01)	–	2.93 (2.31)	0.19 (0.12)	2.56 (0.65)	11.0 (6.5)	2.61 (1.86)	1.59 (0.73)	0.02 (0.01)
AAS-26-D3#1-P7	–	0.01 (0.01)	5.35 (4.45)	0.50 (0.37)	2.54 (0.69)	0.75 (0.48)	22.7 (17.2)	3.60 (1.74)	–
AAS-26-D3#1-P10	–	–	11.7 (10.8)	0.77 (0.64)	6.89 (2.04)	15.1 (10.6)	36.3 (30.6)	7.27 (3.99)	0.02 (0.01)
AAS-26-D3#1-P12	–	–	4.05 (0.38)	0.13 (0.01)	4.08 (0.21)	12.1 (0.6)	4.78 (0.22)	2.12 (0.17)	3.21 (0.23)
AAS-26-D3#1-P14	–	–	2.69 (0.27)	0.08 (0.01)	2.18 (0.13)	15.0 (0.7)	3.96 (0.17)	1.42 (0.12)	3.15 (0.23)
AAS-26-D3#1-P15	–	–	1.68 (0.18)	0.06 (0.01)	1.70 (0.12)	6.15 (0.36)	2.64 (0.13)	1.04 (0.09)	0.27 (0.04)
AAS-26-D3#1-P16	–	–	4.56 (0.48)	0.23 (0.01)	3.69 (0.21)	4.94 (0.31)	25.8 (0.9)	6.01 (0.55)	0.02 (0.01)
AAS-26-D3#1-P18	–	0.01 (0.01)	1.81 (0.22)	0.32 (0.01)	4.58 (0.24)	2.06 (0.15)	15.7 (0.6)	3.76 (0.39)	0.02 (0.01)
AAS-26-D1-I-P2	–	–	3.50 (0.13)	0.72 (0.03)	4.93 (0.23)	4.36 (0.33)	38.9 (1.2)	7.2 (0.27)	0.01 (0.01)
AAS-26-D1-I-P3	–	–	5.48 (0.21)	0.56 (0.03)	4.67 (0.22)	0.85 (0.08)	44.9 (1.3)	8.62 (0.32)	–
AAS-26-D1-I-P4	–	0.02 (0.01)	1.00 (0.04)	0.02 (0.01)	0.03 (0.01)	5.37 (0.41)	0.01 (0.01)	0.01 (0.01)	0.03 (0.01)
AAS-26-D1-I-P6	–	0.01 (0.01)	2.63 (0.12)	0.26 (0.01)	5.57 (0.26)	11.5 (0.9)	11.6 (0.3)	3.98 (0.16)	0.06 (0.01)
AAS-26-D1-I-P8*	–	–	5.39 (0.23)	0.44 (0.02)	6.55 (0.31)	8.09 (0.7)	21.6 (0.6)	5.25 (0.21)	0.01 (0.01)
AAS-26-D1-I-P11	–	0.01 (0.01)	2.64 (0.11)	1.09 (0.06)	4.97 (0.26)	0.91 (0.11)	94.3 (2.9)	15.2 (0.63)	0.01 (0.01)

* indicate cosmic spherules having the presence of platinum group nugget.